The Astrophysical Journal, 667:411–426, 2007 September 20

BROADBAND SPECTRAL EVOLUTION OF SCORPIUS X-1 ALONG ITS COLOR-COLOR DIAGRAM

A. D'Aí
Dipartimento di Scienze Fisiche ed Astronomiche, Universitá di Palermo, Archirafi 36, 90123 Palermo, Italy; dai@fisica.unipa.it

P. Życki
Nicolaus Copernicus Astronomical Center, Bartycka 18, 00-716 Warsaw, Poland

and

T. Di Salvo, R. Iaria, G. Lavagetto and N. R. Robba
Dipartimento di Scienze Fisiche ed Astronomiche, Universitá di Palermo, Archirafi 36, 90123 Palermo, Italy
Received 2006 June 29; accepted 2007 May 7

ABSTRACT

We analyze a large collection of *RXTE* archive data from 1997 April to 2003 August of the bright X-ray source Scorpius X-1 in order to study the broadband spectral evolution of the source for different values of the inferred mass accretion rate by studying energy spectra from selected regions in the *Z* track of its color-color diagram (CD). A two-component model, consisting of a soft thermal component interpreted as thermal emission from an accretion disk and a thermal Comptonization component, is unable to fit the whole 3–200 keV energy spectrum at low accretion rates. Strong residuals in the highest energy band of the spectrum require the addition of a third component that can be fitted with a power-law component, which could represent a second thermal Comptonization from a much hotter plasma, or a hybrid thermal/nonthermal Comptonization. The presence of this hard emission in Sco X-1 has been previously reported, however, without a clear relation with the accretion rate. We show, for the first time, that there exists a common trend in the spectral evolution of the source, where the spectral parameters change in correlation with the position of the source in the CD. In particular, using a hybrid Comptonization model, we show that the power supplied to the nonthermal distribution can be as high as half of the total hard power injected in heating the electron distribution. We discuss the physical implications derived from the results of our analysis, with a particular emphasis on the hardest part of the X-ray emission and its possible origins.

Subject headings: accretion, accretion disks — stars: individual (Scorpius X-1) — stars: neutron — X-rays: binaries — X-rays: general — X-rays: stars

Online material: color figures

1. INTRODUCTION

1.1. *Scorpius X-1*

Scorpius X-1 is the brightest persistent X-ray source in the sky and the first identified X-ray extrasolar source (Giacconi et al. 1962). The X-ray source is an old, low magnetized neutron star (NS), accreting matter transferred through Roche lobe overflow from a low-mass companion (recently identified as an M-class star of $\sim 0.4\ M_{\odot}$; Steeghs & Casares 2002). Sco X-1 is a prototype of the class of the low-mass X-ray binaries (LMXBs), and assuming a distance of 2.8 ± 0.3 kpc (Bradshaw et al. 1999), the source emits close to the theoretical Eddington limit for a $1.4\ M_{\odot}$ NS ($L_{\rm Edd} \sim 2 \times 10^{38}$ ergs s^{-1}).

Based on the timing behavior of LMXBs in correlation with the position of a given source in the X-ray color-color diagram (CD), Hasinger & van der Klis (1989) grouped these sources into two categories: the *Z* sources and the atoll sources. The former are brighter, radiating close to $L_{\rm Edd}$; the latter are less bright, emitting at $0.01L_{\rm Edd}-0.1L_{\rm Edd}$. The *Z* sources exhibit the classical three-shaped branches describing a *Z* pattern in the CD: the horizontal branch (HB) at the top of the *Z* track, followed by the normal branch (NB) and the flaring branch (FB) at the bottom of the pattern. There are strong indications (e.g., Vrtilek et al. 1991) suggesting that what drives the change in the spectral and temporal properties of LMXBs is the instantaneous accretion rate ($\dot{M}$), which, for *Z* sources, is believed to increase monotonically from the HB to the FB. Similarly, atoll sources display two different spectral/timing states: the soft and luminous banana state, associated to higher accretion rates, and the hard and less luminous island state, associated to lower $\dot{M}$. This early and straightforward classification has now moved to a more complex picture, as the patterns that atoll and *Z* sources describe in their CDs, when displayed on long timescales, appear to be more and more similar to each other (Muno et al. 2002; Gierliński & Done 2002), although some observational facts still hold: *Z* sources move on the CDs on shorter timescales, have higher luminosities, and present a timing phenomenology different from that of the atoll sources.

Sco X-1, as all the sources of its class, shows several quasi-periodic oscillations (QPOs) along all the branches of its CD: the horizontal branch oscillations (HBOs), the normal branch oscillations (NBOs), and the flaring branch oscillations (FBOs). In Sco X-1 NBOs, with peak frequencies in the range 4.5–7 Hz, and FBOs, in the frequency range 6–25 Hz, seem to be physically related to each other, since the NBO peak frequency smoothly joins the FBO peak frequency as the source moves from the NB to the FB (Casella et al. 2006). Van der Klis et al. (1996) reported the first observation of HBOs in Sco X-1 at 45 Hz, with an inferred harmonic near 90 Hz; the power spectrum can also show a pair of QPOs, whose frequencies are in the range 800–1100 Hz, denoted kHz QPOs, that shift simultaneously in frequency, with an almost constant or weakly frequency-dependent peak separation (see, e.g., Zhang et al. 2006). The physical interpretation of these timing features is not unique, and the related scientific debate is still open (see van der Klis 2006 for a review).

Spectral studies of Sco X-1 have been so far not so extensive and detailed as timing studies. This is in part due to the strong

brightness of the source that actually prevents its observation with the most sophisticated and high-resolution X-ray satellites like *BeppoSAX* and *ASCA* in the recent past, and *Chandra* and *XMM-Newton* at present. Three articles have investigated so far the broadband spectral behavior of the source, using data from the *Rossi X-Ray Timing Explorer* (*RXTE*). Barnard et al. (2003) used data from both the Proportional Counter Array (PCA) and the High Energy X-Ray Timing Experiment (HEXTE), showing that the spectrum, in the energy range 2.5–50 keV, can be fitted by a simple two-component model, a blackbody soft component and a cutoff power law, plus a broad Gaussian line, and interpreted these results in the framework of the so-called Birmingham model (Church & Balucińska-Church 2001). In this interpretation the spectral emission consists of blackbody emission from the NS plus Comptonized emission from an extended accretion disk corona. Bradshaw et al. (2003) used only PCA data (in the 2.5–18.2 keV range), adopting a model consisting of a blackbody emission plus a bulk motion Comptonization component and a reflection component in the form of a broad Gaussian line. D'Amico et al. (2001) studied HEXTE data above 20 keV, in order to test the presence of high-energy X-ray emission in the spectra of the source. Data were fitted, using a bremsstrahlung component, to mimic the effects of the thermal component, and a power-law component, whenever the statistics and clear residuals in the fit required it. In this way no apparent correlation was found between the presence of the hard tail and position of the source in the CD, contrary to what had been reported for other *Z* sources.

More recently, Di Salvo et al. (2006), using *INTEGRAL* data in the 20–200 keV energy band, detected a hard X-ray tail, with photon index values between 2 and 3.4, whose intensity decreased as the source moved toward higher accretion rates. Data did not show evidence of a high-energy cutoff up to $\sim$200 keV, suggesting a nonthermal origin for the hard tail.

Sco X-1 is also an interesting source of radio emission. Fomalont et al. (2001) through an extensive Very Long Baseline Array monitoring campaign, have shown that the radio emission is composed of a pointlike radio core emission at the position of the X-ray source and of two opposite radio lobes, moving through the interstellar medium with relativistic speeds $v/c = 0.45 \pm 0.03$, and with an angle of $46^\circ \pm 6^\circ$ with respect to our line of sight. Also evident is a connection between the phenomenon of radio flare at the core of the source and the following flaring of the lobes. It is argued, thereafter, that the energy production of the radio emission is confined near the NS and only afterward transported to the lobes via the working surface of a jet (see, e.g., the magnetohydrodynamic simulations of Kato et al. 2004).

These results stimulated the search for the possible connection between inflow and outflow mechanisms working in the violent regimes of accretion onto a NS or a black hole (BH). Energetic mass outflows, collimated sometimes in a typical jet pattern, can be produced not only in extragalactic X-ray sources, such as quasars and active galactic nuclei, but also in galactic X-ray binary systems (see Fender 2002 for a review). It has been observed that galactic BH binary systems are able to produce strong jet emission (sources for which a jet has been already spatially resolved are usually denoted *microquasars*), with radio-loud states associated to hard/low X-ray states, alternated to periods of radio quenching during soft/high X-ray states. For NS systems radio-loud episodes are generally interpreted as a jet signature. In this context, all the *Z* sources seem to have, under certain conditions, a radio-jet nature. Detections of radio-loud states are usually associated with spectral states of low $\dot{M}$, i.e., on the HB of the *Z* track (Fender & Hendry 2000), while the few radio detections in atoll systems found the sources residing in the island state of their CDs (Migliari et al. 2003).

1.2. *Spectral Properties of Z Source Class*

We rapidly review in this section the spectral properties of the *Z* sources. The class of the *Z* sources display a homogeneous pattern of spectral properties; their energy spectra can be usually decomposed as follows:

1. A soft thermal component, with characteristic temperatures in the 0.5–1 keV range, interpreted as thermal emission from the NS surface or an optically thick, geometrically thin accretion disk;
2. a thermal Comptonized component, where the electron cloud distribution has a temperature in the 2.5–3 keV range, the soft seed photon temperature is around 1 keV, and the optical depth can have rather large values ($\tau \geq 3$); this relatively cold thermal Comptonization is thought to take place close to the NS surface; the soft seed photon temperature generally exceeds the highest temperature reached in the accretion disk, so that the source of the soft emission is probably confined in the boundary layer between the inner edge of the accretion disk and the NS surface. The high optical depth values associated to the cloud saturates the seed photon spectrum close to the electron temperature, so that a quasi-Wien spectrum results. A theoretical interpretation of this spectral decomposition has been given by Inogamov & Sunyaev (1999), where the boundary layer emission is expected to be radiation pressure supported and its emission is locally at the Eddington rate. Change in luminosity is attributed to a change in the emitting area rather than in its emissivity. Phase-resolved spectroscopy of bright LMXBs (Revnivtsev & Gilfanov 2006) further supports this interpretation, establishing in all the analyzed *Z* sources a common cutoff, due to the boundary layer thermal emission, at $\simeq$2.4 keV.
3. a reflection component, often simply modeled with a broad Gaussian line, in the 6.4–6.9 keV range. In all the *Z* sources this line has been always observed; spectra from *BeppoSAX* or *RXTE* observations were not able to constrain the shape of the line, while the relative width was in the range 0.1–1 keV. High-resolution spectra in this energy range have been obtained so far only with the BBRXT (Broad Band X-Ray Telescope; Smale et al. 1993) and the *XMM-Newton* satellites (Costantini et al. 2005) for Cygnus X-2; in both observations the line was associated to highly ionized iron (centroid energy $\simeq$6.7 keV), while the line appears to be intrinsically broad (FWHM $\sim$ 1 keV). Brandt & Matt (1994) pointed out that the determination of the line profile can be a primary diagnostic tool, but, at the same time, kinematic and relativistic effects can greatly distort the line from the simple Gaussian profile. Moreover, if reflection is caused by hard X-rays reflected by a cold accretion disk, the contribution of the Compton-reflected continuum should be taken into account, when the iron line emission is a considerable contribution to the total energy flux; and
4. a power-law hard tail, which can contribute up to few percent to the total energy flux, whose strength usually varies in correlation with the position of the source in the CD, namely being the strongest on the HB, gradually decreasing as the source moves to higher accretion rates and totally fading in the FB (e.g., GX 17+2; Di Salvo et al. 2000). The photon index of the power law was generally found in the range 1.5–3 with no evident high-energy cutoff up to energies of about 200 keV.

In this article we report a complete investigation of the spectral properties of Sco X-1 through an extensive analysis of *RXTE*

TABLE 1
Log of the *RXTE* Observations Used in the Analysis

Proposal Number (CD)	Starting Time (TT)	Ending Time (TT)	Effective Time (ks)
20035A	1997 Apr 18, 15:20:32	1997 Apr 24, 19:02:40	75.6
20035B	1998 Jan 3, 21:17:52	1998 Jan 8, 13:19:44	60.0
30036	1998 Jan 7, 13:29:52	1998 Jan 8, 22:16:48	30.4
30035A	1998 May 30, 00:28:00	1998 Jun 2, 07:01:36	47.8
30035B	1998 Jul 2, 06:26:40	1998 Jul 5, 10:32:00	32.2
40020	1999 Jan 6, 05:25:20	1999 Jan 16, 23:34:40	122.1
70014	2002 Mar 15, 01:02:56	2002 May 16, 23:20:32	139.0
70015	2002 May 19, 21:55:44	2002 May 19, 23:54:40	2.24
80021	2003 Jul 30, 03:00:48	2003 Aug 13, 16:43:44	146.9

Notes.—Observation log of the *RXTE* data sets used for our analysis. Some data sets, although having the same proposal number, contain pointed observation separated by long time intervals. In these cases we collected all the pointing observations close in time in just one CD, and distinguish the relative CDs by a letter, following the proposal number. Starting and ending times are expressed in Terrestrial Time (TT). Effective exposures times are filtered by our GTI screening criteria.

archive data, indicating a clear connection between position of the source on the CD and spectral behavior.

2. DATA REDUCTION AND ANALYSIS

The scientific payload of *RXTE* consists of three instruments: the PCA, the HEXTE, and the All-Sky Monitor (ASM). The PCA consists of five co-aligned Xenon proportional counter units (PCUs) with a total effective area of about 6500 cm^2. The instrument is sensitive in the energy range from 2 up to 60 keV (Jahoda et al. 1996), although the response matrix is best calibrated in the energy range 3–22 keV. Data can be processed using several different configuration modes; for our analysis we exclusively use the Standard2 mode, with 16 s time resolution and 128 energy channels in the 2–60 keV energy range. The HEXTE consists of two clusters of four Na I/Cs I–phoswich scintillation counters that are sensitive from 15 up to 220 keV (Rothschild et al. 1998). We use the Standard Mode , with 64 energy channels, for the reduction and analysis of the HEXTE data. Background subtraction is done by using the source-background rocking of the collimators. We use HEXTE response matrices of 1999 August.

We collected a large amount of *RXTE* archive data, discarding only minor shorter observations, from 1997 April up to 2003 August. We present in Table 1 the data sets we used for our analysis, indicating the associated proposal number, the starting and ending times of each observation in Terrestrial Time, and the corresponding exposure times.

Data have been processed using the standard selection criteria, discarding data taken during Earth occultations and passages through the South Atlantic Anomaly. We only used data from PCU2 for the PCA and data from Cluster A for the HEXTE instrument. We constructed color-color diagrams (CDs) of the source by extracting energy-dependent light curves using PCA energy channels 5–10, 11–16, 17–22, and 23–44, with a 64 s bin time. These channel ranges correspond to the energy ranges 1.94–4.05, 4.05–6.18, 6.18–8.32, and 8.32–16.26 keV, respectively. We define the soft color (SC) as the ratio of count rates in the 4.05–6.18 and 1.94–4.05 keV energy bands, while the hard color (HC) is defined as the ratio of count rates in the 8.32–16.26 and 6.18–8.32 keV energy ranges. However, the channel-to-energy conversion depends on the period of activity of the satellite (there are five different instrumental epochs): most of our data belong to epoch 3, for which the given energy bands are appropriate; for the epoch 5 data sets the energy ranges are slightly shifted, so that this results in a consequent shift on the HC and on the SC axes. Because we are not interested in the secular shifts of the track in the CD, nor do we want to accumulate spectra taken at different epochs, but to perform a statistical study of the broadband spectral behavior of the source for different CD positions in different data sets, we did not perform the energy-dependent corrections to the colors.

We selected regions in the CDs for each observation data set, in order to cover a homogeneous part of the *Z* track and to have at the same time a suitable statistics. From these selections we derived the good time intervals (GTIs), which we used for extracting the corresponding spectra for the PCA and HEXTE data.

Given the high luminosity of the source all the PCA spectra have been dead-time corrected. Some observations were performed with the use of an offset pointing; in these cases we extracted the responses matrixes of both the HEXTE and the PCA instruments, following the indications given in the online data analysis documentation pages. We processed and analyzed data using version 6.0 of the FTOOLS package suite and version 11.3.1 of XSPEC.

3. THE DATA

Hereafter we refer to a collection of close in time pointed observations used to extract one CD by using its proposal number. From data sets 20035 (and 30035) we have obtained two different CDs; we label them 20035A and 20035B, respectively (30035A and 30035B; see the Spectrum column in Table 2). Data sets 20035A, 20035B, 30036, 30035A, 30035B, and 40020 belong to epoch 3, while data sets 70014, 70015, and 80021 belong to epoch 5. Data sets 70014 and 70015 have been merged in one CD, because these observations were close in time and the source pointing was the same.

The eight CDs that we have extracted present the source mostly on the NB/FB, as these are the states where the source spends most of the time. In Sco X-1 the HB is not *horizontal* but rather a vertical continuation of the NB (a characteristic shared also by GX 17+2 and GX 349+2, the so-called Sco-like sources). For visual clarity we refer to the Sco X-1 CD pattern, mainly making the distinction between the left (or FB) track and the right (NB and HB) track, and between the top (harder) parts and the bottom (softer) parts of the tracks.

The count rates associated with the extracted spectra show a significant trend, generally correlated with the HC; HEXTE and PCA count rates are the highest at the top of the FB and monotonically decrease toward the FB/NB apex; following the direction bottom NB → HB, the trend is inverted. This behavior

TABLE 2
COLOR-DIAGRAM-RESOLVED SPECTRA AND FITS RESULTS

SPECTRUM (No. + Data Set)	EXPOSURE (s)	COUNT RATES (counts s^{-1})		ENERGY RANGE (keV)		dbbtt χ^2_{red} (dof)	dbbttpeg χ^2_{red} (dof)	dbbeqpair χ^2_{red} (dof)
		PCA	HEXTE	PCA	HEXTE			
01 20053A	5728	20920	621	3–22	20–200	0.63 (62)	0.59 (61)	...
02 20053A	22400	18600	521	3–22	20–200	1.46 (62)	0.80 (60)	0.85 (61)
03 20053A	9163	19760	651	3–22	20–200	1.07 (62)	0.62 (61)	...
04 20053A	11040	20550	736	3–22	20–200	2.53 (62)	0.55 (60)	0.55 (61)
05 20053A	8576	21060	848	3–22	20–200	2.84 (62)	1.14 (60)	1.14 (61)
06 20053A	13472	21740	1015	3–22	20–200	5.62 (62)	0.64 (60)	0.63 (61)
07 20053B	5698	27960	1675	3–22	24–200	2.12 (59)	1.21 (58)	1.27 (57)
08 20053B	9680	25820	1054	3–22	20–200	1.89 (62)	0.99 (60)	1.04 (60)
09 20053B	11472	21870	642	3–22	20–200	1.03 (62)	0.93 (60)	...
10 20053B	13920	19320	512	3–22	20–200	1.35 (62)	0.54 (60)	...
11 20053B	18720	19930	613	3–22	20–200	1.65 (62)	0.68 (60)	0.55 (61)
12 30036	4208	28590	1840	3–22	24–200	2.39 (59)	1.41 (58)	1.40 (57)
13 30036	4336	26930	1271	3–22	22–200	1.91 (61)	1.32 (60)	1.42 (60)
14 30036	7072	23480	799	3–22	20–200	0.85 (62)	0.86 (61)	...
15 30036	4736	19130	492	3–22	20–200	0.60 (62)	0.59 (61)	...
16 30036	10320	20000	633	3–22	20–200	2.36 (62)	0.65 (60)	0.67 (61)
17 30035A	6880	23680	84	3–22	24–200	1.11 (59)	1.07 (58)	...
18 30035A	6608	19260	43	3–22	24–200	0.69 (59)	0.68 (58)	...
19 30035A	8704	17380	39	3–22	24–200	1.17 (59)	0.87 (58)	...
20 30035A	15456	18020	50	3–22	24–200	2.62 (59)	0.71 (57)	0.72 (58)
21 30035A	10064	20040	92	3–22	24–200	2.84 (59)	0.50 (57)	0.53 (58)
22 30035B	3344	24310	100	3–22	24–200	1.03 (59)	1.04 (58)	...
23 30035B	7344	16770	39	3–22	22–200	1.06 (61)	1.08 (60)	...
24 30035B	4976	16520	43	3–22	22–200	1.12 (61)	0.99 (60)	...
25 30035B	16144	18900	76	3–22	24–200	2.56 (59)	0.49 (57)	0.44 (58)
26 40020	3401	23380	708	3–22	24–200	1.86 (59)	0.83 (57)	0.86 (58)
27 40020	3642	20360	544	3–22	20–200	1.26 (62)	0.81 (60)	...
28 40020	18493	15810	300	3–22	20–200	1.14 (62)	0.69 (60)	...
29 40020	11967	14920	286	3–22	20–200	1.29 (62)	1.18 (61)	...
30 40020	5735	16100	383	3–22	20–200	0.85 (62)	0.67 (61)	...
31 40020	7537	17100	470	3–22	20–200	3.59 (62)	0.70 (60)	0.66 (61)
32 70014	822	24440	948	3–22	22–200	1.16 (58)	0.91 (56)	...
33 70014	5668	18740	368	3–22	20–200	1.24 (58)	0.72 (56)	...
34 70015	976	15250	280	3–22	20–200	0.63 (58)	0.63 (57)	...
35 70015	1248	16300	363	3–22	20–200	0.75 (58)	0.69 (57)	...
36 70014	3804	17570	447	3–22	22–200	1.42 (58)	0.73 (56)	0.72 (57)
37 80021	5344	13030	12.8	3–22	28–200	0.73 (53)	0.59 (52)	...
38 80021	6752	9900	2.0	3–22	28–200	0.60 (53)	0.46 (52)	...
39 80021	17312	8828	7.6	3–22	28–200	0.54 (53)	0.51 (52)	...
40 80021	14624	9071	27.0	3–22	28–200	0.64 (53)	0.57 (52)	...
41 80021	29504	8990	11.7	3–22	28–200	1.27 (53)	0.78 (52)	...
42 80021	30384	10320	6.6	3–22	28–200	1.37 (53)	0.67 (53)	0.70 (52)
43 80021	18656	10730	11.0	3–22	28–200	1.57 (53)	0.74 (53)	0.69 (52)

NOTES.—We report in this table, from left to right, the chosen identifying number of the CD-selected spectra (as shown in Fig. 1) together with the associated observational data set, its exposure times, the relative background-subtracted count rates for the PCA and HEXTE, the energy band considered in the fits, and the reduced χ^2 values obtained from the fits, adopting the dbbtt, the dbbttpeg, and the dbbeqpair model; the degrees of freedom (dof) for each fit are shown in parentheses.

is mostly stressed in the HEXTE data (compare the count rate in spectrum 07 in the top FB with spectrum 10 in the transition region FB/NB, for which the rate is reduced by two-thirds in the HEXTE, but only by one-third in the PCA).

In four data sets (20035A, 20035B, 40020, and 30036) the satellite pointed the source on-axis; in three data sets (30035A, 30035B, and 80021) an offset pointing has been used. This influenced the high-energy statistics, where in the same position on the CD, an offset pointing produced an HEXTE count rate lowered by almost 1 order of magnitude. Spectra extracted from data sets 70014 and 70015 also have low statistics in the HEXTE band, as the integration time is shorter compared with the other spectra.

We generally used a 3.0–22 keV energy band for the PCA spectra and a 20–200 keV energy band for the HEXTE spectra. HEXTE channels from 28 to 63 have been rebinned, grouping four channels into one. In some of the spectra that we extracted we found, however, model-independent mismatches in the overlapping energy region between the HEXTE and the PCA; because these mismatches are of instrumental origin we occasionally restrict these energy bands until these features no longer impacted our fit results. In Table 2 we report the exact energy bands used for the PCA and the HEXTE data sets for the selected spectra.

The choice to assign an appropriated systematic error for the PCA data is an essential step in the analysis of the spectra. This

operation is not straightforward, as the commonly used standard candle, the Crab, provides in this case only a partial calibration tool. The Crab count rate for every energy channel below ~20 keV is about 1 order of magnitude less than the Sco X-1 count rate, thus making the extrapolation of the Crab-based systematic error to the Sco X-1 spectra risky. The most adopted view to assign a 1% systematic error for all the energy channels has a strong impact on the softer part of the spectrum, where there are the most weighted channels; we found that in this case the fit is strongly driven by residuals in the 3–6 keV range, leading to a modelization of the spectrum that does not seem physically plausible. The overall effect is a shift of any soft component outside the *RXTE* energy band, and unrealistic high values for the extrapolated flux.

The only way to avoid the strong driving effect of the first channels is to arbitrarily raise the systematics in this range; we found that assigning a 3% systematic error for channels between 3 and 3.9 keV (namely the first two PCA channels available in our spectra), while leaving a 1% systematic error for all the other channels, allows us to derive a physically plausible scenario for the spectral evolution of the source, does not result in extreme lower/higher values of reduced χ^2 for every fit performed, and allows us to exploit all the available energy band and to generally constrain all the spectral components of the adopted models. We occasionally still found in some fits systematical residuals in the soft part of the spectrum, that are more stressed in the softer spectra, whose origin can be presumedly instrumental and related to the Xenon L edge near 5 keV. We choose to ignore these effects, in order to not overparameterize the fit, as they do not influence the determination of the spectral parameters and do not impact the χ^2 values of the fits.

No systematic error has been associated to the HEXTE data. A normalization constant is left free to vary between the PCU2 and HEXTE spectra to take into account residual flux calibration uncertainties.

4. SPECTRAL MODELS

As pointed out in § 1, spectra of LMXBs are usually described as the sum of at least two spectral components. Because the PCA energy band starts from 3 keV, it is not possible to constrain the effect of the photoelectric interstellar absorption on the source flux. Following Christian & Swank (1997) we fixed its value to 3×10^{21} cm^{-2}, for each fit performed. To fit the CD-selected spectra, we tried at first a series of models given by the combination of a soft thermal component, such as a blackbody or multicolor disk blackbody (`diskbb` in XSPEC; Mitsuda et al. 1984), and a thermal Comptonized component. For the latter we, alternatively, tried the `compps` (Poutanen et al. 1996), `comptt` (Titarchuk 1994), and `thcomp` (not included in the standard XSPEC package; see Zdziarski et al. 1996) Comptonization models. For any model adopted, large residuals in the 6–10 keV energy range indicated the presence of iron features, which we simply modeled with a broad Gaussian line in the 6–7 keV energy range. We noted a general tendency for any adopted model to have a very broad Gaussian line (with $\sigma \geq 0.8$ keV) and, generally, with centroids at energies $\leq$6.4 keV. In order to avoid unrealistically large Gaussian lines, absorbing the continuum underneath, we constrained the line to have centroid energies only in the 6.4–7.0 keV energy range, with a line width less than 0.8 keV, while the normalization of the line was a completely free to vary parameter.

We found an adequate description of the data, for energies below 30 keV, using a two-component model given by the combination of the `diskbb` and the `comptt` components, a modelization that was first introduced by Mitsuda et al. (1984) and that is known as the *Eastern model*. Other Comptonization models can also statistically equally well represent the spectral sample, but we preferred to illustrate our results using this Compton model, as it is one of the most used in the LMXB spectral analysis and allows an easy way to compare our results with results obtained for other sources.

Using the other often used modelization, the Western model (White et al. 1986), which predicts a ~1–2 keV blackbody thermal emission and a Comptonization component with disk soft seed photon in the 0.4–0.8 keV energy range (see, e.g., Barnard et al. 2003), we found higher χ^2 values for each spectrum and an extrapolated super-Eddington luminosity along each part of the *Z* track that would be dramatic for some FB spectra, which would overcome by more than an order of magnitude the Eddington limit, thus making this assumption not realistic. Moreover, the power dissipated in the Comptonizing disk corona would be constantly much greater than the power dissipated as thermal emission on the NS surface, and this breaks our expectations that the power dissipated near the compact object should be at least of the same order of the power dissipated along the disk, if the disk is very close to the NS (see also Done et al. 2002, for a more extensive discussion).

The `diskbb` has two free parameters: the temperature expressed in keV at the inner disk radius ($kT_{\rm DB}$) and a normalization factor that depends on the inner radius of the accretion disk, the distance from the source, and the inclination angle between the line of sight and the normal to the disk; the `comptt` has four free parameters: the soft seed photon temperature, kT_0; the electron temperature of the Comptonizing cloud, kT_e; the optical depth, τ; and a normalization constant. We assumed that the Comptonizing geometry is spherical. We refer to this two-component model as the `dbbtt` model.

As is evident from Table 2 the `dbbtt` model is, however, gradually unable to satisfactorily fit the whole energy spectrum, as the source resides in zones of low inferred accretion rate. The residuals, with respect to this model, clearly indicated an excess of flux at energies greater than 30 keV. There is also a second group of spectra (namely spectra 7, 8, 12, 13, and 26) that gave for the same reason an unsatisfactory high χ^2 value. These spectra lie at the top of the FB in the data sets that have the higher HEXTE statistics. We refer to this particular set as the top-FB spectra.

Because the mechanisms producing this hard excess in the *Z* sources are not clear yet, in the following we adopt two working hypotheses to fit the broadband continuum of the source: (1) as in the case of the quasi-saturated boundary layer Comptonization, this component is also the result of a thermal Comptonization process, but from a much hotter plasma; and (2) a broadband spectrum is the result of a hybrid electron velocity distribution, i.e., a thermal electron distribution, which produces the optically thick Comptonization, with a power-law nonthermal tail that is responsible for the high-energy excess. Because, for case (1), the hot plasma can only reside in regions close to the central compact object, where magnetic and gravitational effects are the strongest, we assume that the boundary layer radiation field is the primary source of soft seed photons also for this second thermal Comptonization. We note that this assumption is also needed in order to avoid an overestimation of the contribution of steep hard tail at low energies. The use of an unbroken power law at steep photon indices can give a major contribution in the lowest energy band of the spectrum, so that the fit is driven by low-energy residuals, possibly resulting in an erroneous continuum modelization. Thereafter, a low-energy cutoff at the seed photon temperature must be taken into account, as the expected photon field spectrum is within the instrumental range.

We added, thereafter, to our basic two-component model, a power law in order to mimic this second Comptonization, multiplied by a low-energy cutoff. We set the value of the low-energy cutoff anchored to the kT_0 value of the `comptt` component, while we choose the power law to have a pegged normalization expressed as flux of this component in the 20.0–200.0 keV energy range (`pegpwrlw` in XSPEC). We checked for each spectrum the χ^2 improvement by adding a high-energy cutoff, noting that we could obtain only lower limits on the cutoff energy, generally in the 30–100 keV range without any significant improvement in the χ^2. Thereafter we did not use a high-energy cutoff. We refer at this model simply as `dbbttpeg` or the *two Comptonizations* model.

To model the possibility given in case (2) we also fitted the spectra showing a strong hard excess (namely spectra for which the `dbbtt` model gave a null hypothesis probability less than 0.05; it generally corresponded to a reduced χ^2 value of 1.4) with a model given by the sum of a thermal disk component plus the recently developed thermal/nonthermal hybrid Comptonization model named EQPAIR (see Coppi [1999, 2000] for a full description of the model). It embodies Compton scattering, $e^{\pm}$ pair production and annihilation, $pe^{\pm}$ and $e^{\pm}e^{\pm}$ thermal and nonthermal bremsstrahlung, and energy exchange between thermal and nonthermal parts of the $e^{\pm}$ distribution via Coulomb scattering. Selected electrons are accelerated to suprathermal energies, and the thermal part of the $e^{\pm}$ distribution can be additionally heated. This model assumes a spherical plasma cloud with isotropic and homogeneous distribution of photons and $e^{\pm}$, and soft seed photons produced uniformly within the plasma, with a thermal temperature of $kT_{\rm BB}$. The properties of the plasma depend on its compactness, $l \equiv \mathcal{L}\sigma_{\rm T}/(\mathcal{R}m_e c^2)$, where $\mathcal{L}$ is the total power in the source, $\mathcal{R}$ is the radius of the sphere, and $\sigma_{\rm T}$ is the Thomson cross section. The compactness is divided in a hard compactness, l_h, which corresponds to the power supplied to the electrons, and a soft compactness, l_s, corresponding to the power supplied in the form of soft photons. The compactnesses corresponding to the electron acceleration and to the additional heating of the thermal part of the $e^{\pm}$ distribution are denoted as $l_{\rm nth}$ and $l_{\rm th}$, respectively, and $l_{\rm h} \equiv l_{\rm nth} + l_{th}$. The nonthermal energy distribution of the electrons in the plasma is assumed to be a power law replacing the Maxwellian exponential tail from a gamma Lorentz factor $\gamma_{\rm min} = 1.3$ up to a $\gamma_{\rm max} = 1000$ with an energy index $G_{\rm inj}$. The total Thomson optical depth and the electron temperature of the plasma are computed self-consistently from the assumed optical depth τ_p of the background electron-proton plasma.

We choose to model the thermal disk emission using as in the hot Comptonization model the `diskbb` component for spectra in HB/NB, while we adopted the post-Newtonian model `diskpn` (Gierliński et al. 1999) in the case of the topFB spectra, as, in this accretion state, we expect the disk to reach its minimum inner disk radius, close to the NS; the `diskpn` model takes into account the effective gravitational potential in the neighborhood of the compact object by computing the emergent disk spectrum using a more appropriate post-Newtonian potential. We assumed that the disk reaches the last stable orbit at $6R_g$ and fixed this parameter for the fits performed, while we left free to vary the maximum disk temperature ($T_{\rm max}$) and a normalization factor [$K = M^2 \cos(i)/D^2\beta^4$, where M is the central mass expressed in solar units, i is the inclination of the disk, D is the distance to the source in kiloparsecs, and β is the color/effective temperature]. We have left free to vary for the EQPAIR component the following parameters: $kT_{\rm BB}$, l_h/l_s, $l_{\rm nth}/l_h$, τ_p, and the normalization factor. The $G_{\rm inj}$ was not very sensible to variations in the range between 1.5 and 3 for spectra in the HB/NB, while for the topFB spectra had to be left as a free to vary parameter, as this gave a significant decrease in the χ^2 when left as a free to vary parameter. The value of the soft compactness l_s was unconstrained by the fit (it is mainly driven by the pair production rate, which manifests itself with the annihilation line at energies $\simeq$500 keV, obviously far beyond our energy limits), and we kept it frozen at the value of 10 (see also Gierliński et al. 1999). All the other parameters of the model were frozen at the default values. We refer to this modelization as the `dbbeqpair` model, or simply, the *hybrid Comptonization* model.

5. RESULTS AND DISCUSSION

We have examined 43 energy spectra of Sco X-1 in the 3.0–200 keV energy band using *RXTE* pointed observations from 1997 April to 2003 August; the spectra have been extracted from selected regions chosen in the X-ray CD. We produced a CD for each close in time data set in order to avoid shifts of instrumental origin, and repeated our analysis for each CD obtained in this way, thus having at hand a robust representation of the spectral evolution of the source in all its accretion states.

To fit the spectra we first adopted a two-component model given by the sum of a soft thermal disk emission and a hard Comptonized emission. We checked for the presence of harder X-ray emission by adding a high-energy power law to our basic model, while for a subset of spectra we adopted a hybrid thermal/nonthermal Comptonization as described in the previous section.

We find that the basic two-component model `dbbtt` can fit the 3–200 keV energy band spectrum (fits for which we obtained a $\chi^2_{\rm red} \leq 1.4$) in 25 out of a total 43 spectra; these spectra mostly belong to the FB and to the NB. Hard tails, in this group of spectra, are not significantly detected in 14 spectra (these are spectra 1, 9, 14, 15, 17, 18, 22, 23, 24, 29, 34, 35, 39, and 40; see Table 2) when the source lies in the FB/NB apex of its CD. For the other 11 spectra, although the addition of a new component is not strictly required by the fit, we found a general improvement in the χ^2 value.

On the contrary, we find that this model fails to describe the spectra in 18 of the 43 selected spectra (fits for which we obtained a $\chi^2_{\rm red} \geq 1.4$); the fits generally getting worse and worse from the bottom of the FB to the upper NB. From the residuals with respect to this model, it is clearly seen that there is an excess of hard emission at energies above 30 keV. We report in Figure 9 four representative deconvolved spectra for the case in which the `dbbtt` model does not give an adequate description to the broadband spectral behavior, choosing three spectra from the HB/NB zone and one for the topFB zone: spectrum 06 (at the top of the left track of data set 20035A), spectrum 16 (at the top of the left track of data set 30036), spectrum 31 (at the top of the left track of data set 40020), and spectrum 07 (at the top of the right track of data set 20035B).

In the following we group the spectra according to the relative position in their CDs, in: topFB spectra (spectra 7, 8, 12, 13, 17, 22, 26, 32, and 37); FB spectra (1, 9, 14, 18, 27, 28, 33, and 38); NB spectra (2, 3, 10, 15, 19, 20, 23, 24, 29, 30, 34, 35, 39, and 40); and HB spectra (4, 5, 6, 11, 16, 21, 25, 31, 36, 41, 42, and 43). We caution the reader that this distinction is based only on the results of our spectral analysis for spectra taken in particular zones of the Z track, without any reference to the temporal behavior of the source. Although it is clear, looking just at the light curves, to distinguish within one data set the FB from the NB, the distinction between the NB and the HB is rather subtle, as the

TABLE 3

Fit Results: Thermal Comptonization Model

Parameter	kT_{DB} (keV)	R_{DB} (km)	E_{Gaus} (keV)	σ_{Gaus} (keV)	N_{Gaus} (photons cm^{-2} s^{-1})	T_0 (keV)	T_e (keV)	τ	Index	F_{PEG} (ergs cm^{-2} s^{-1})	F_{TT} (ergs cm^{-2} s^{-1})
1	$1.62^{+0.07}_{-0.07}$	$12.9^{+1.1}_{-1.0}$	$6.45^{+0.16}_{-0.05}$	$0.42^{+0.3}_{-0.4}$	$0.18^{+0.08}_{-0.06}$	$2.34^{+0.07}_{-0.05}$	$3.8^{+11}_{-1.6}$	5^{+5}_{-3}	2	170^{+120}_{-120}	7.90
2	$1.47^{+0.04}_{-0.02}$	$15.5^{+0.5}_{-0.9}$	$6.49^{+0.13}_{-0.09}$	$0.54^{+0.24}_{-0.25}$	$0.17^{+0.04}_{-0.05}$	$2.23^{+0.04}_{-0.02}$	$3.4^{+0.8}_{-0.3}$	$7^{+1.7}_{-2.7}$	$2.3^{1.6}_{-0.5}$	300^{+50}_{-50}	7.28
3	$1.43^{+0.06}_{-0.06}$	$16.4^{+1.6}_{-1.4}$	$6.50^{+0.21}_{-0.13}$	$0.66^{+0.14}_{-0.3}$	$0.19^{+0.08}_{-0.08}$	$2.27^{+0.03}_{-0.21}$	$4.3^{+9}_{-0.6}$	4^{+3}_{-2}	2	360^{+80}_{-80}	8.76
4	$1.37^{+0.10}_{-0.12}$	$17.8^{+3}_{-2.5}$	$6.48^{+0.23}_{-0.08}$	$0.7^{+0.07}_{-0.5}$	$0.21^{+0.11}_{-0.11}$	$2.20^{+0.21}_{-0.24}$	$3.4^{+1.1}_{-0.4}$	7.8^{+4}_{-3}	$1.6^{+0.4}_{-0.3}$	670^{+80}_{-80}	10.1
5	$1.43^{+0.08}_{-0.11}$	$16.5^{+3.0}_{-2.0}$	$6.50^{+0.26}_{-0.10}$	$0.64^{+0.16}_{-0.6}$	$0.16^{+0.11}_{-0.08}$	$2.35^{+0.09}_{-0.12}$	$3.8^{+1.1}_{-0.5}$	$5.9^{+2.7}_{-2.7}$	$1.5^{+0.2}_{-0.5}$	710^{+90}_{-90}	10.4
6	$1.48^{+0.04}_{-0.03}$	$15.0^{+1.8}_{-1.0}$	$6.51^{+0.23}_{-0.11}$	$0.45^{+0.4}_{-0.4}$	$0.12^{+0.08}_{-0.05}$	$2.51^{+0.03}_{-0.02}$	$5.45^{+0.5}_{-1.0}$	$2.96^{+1.9}_{-0.13}$	$1.5^{+0.2}_{-0.2}$	980^{+80}_{-80}	11.2
7	$2.12^{+0.07}_{-0.19}$	$8.5^{+1.3}_{-1.6}$	$6.40^{+0.17}$	$0^{+0.5}$	$0.08^{+0.03}_{-0.04}$	$2.92^{+0.01}_{-0.01}$	10	$0.02^{+0.06}_{-0.01}$	$0.3^{+0.5}_{-0.3}$	730^{+180}_{-180}	10.8
8	$2.04^{+0.04}_{-0.03}$	$9.2^{+0.3}_{-0.1}$	$6.40^{+0.18}$	$0^{+0.4}$	$0.09^{+0.04}_{-0.03}$	$2.80^{+0.01}_{-0.02}$	10	$0.01^{+0.18}_{-0}$	$0.5^{+0.5}_{-0.5}$	500^{+130}_{-120}	7.76
9	$1.64^{+0.06}_{-0.09}$	$12.5^{+1.0}_{-1.0}$	$6.44^{+0.16}_{-0.17}$	$0.3^{+0.3}_{-0.3}$	$0.14^{+0.07}_{-0.05}$	$2.34^{+0.06}_{-0.05}$	$3.9^{+2}_{-0.6}$	5^{+5}_{-3}	$0.2^{+1.0}_{-0.2}$	260^{+80}_{-90}	7.53
10	$1.39^{+0.05}_{-0.05}$	$16.3^{+1.3}_{-1.0}$	$6.49^{+0.17}_{-0.17}$	$0.5^{+0.3}_{-0.3}$	$0.20^{+0.08}_{-0.06}$	$2.12^{+0.04}_{-0.04}$	$3.6^{+2.1}_{-0.4}$	$6.3^{+2.0}_{-2.3}$	$1.5^{+0.5}_{-0.5}$	390^{+80}_{-80}	8.3
11	$1.44^{+0.03}_{-0.06}$	$16.5^{+2.5}_{-1.5}$	$6.52^{+0.18}_{-0.12}$	$0.57^{+0.2}_{-0.3}$	$0.17^{+0.08}_{-0.06}$	$2.32^{+0.05}_{-0.05}$	$4.50^{+2.0}_{-0.05}$	$3.89^{+3.7}_{-0.15}$	$1.4^{+0.5}_{-0.2}$	390^{+70}_{-70}	11.4
12	$2.07^{+0.09}_{-0.09}$	$8.7^{+0.5}_{-0.7}$	$6.40^{+0.18}$	$0^{+0.5}$	$0.09^{+0.04}_{-0.05}$	$2.93^{+0.02}_{-0.07}$	10	$0.01^{+0.16}$	$0.7^{+0.6}_{-0.6}$	560^{+160}_{-150}	12.1
13	$2.06^{+0.05}_{-0.05}$	$9.0^{+0.5}_{-0.4}$	$6.40^{+0.21}$	$0^{+0.5}$	$0.09^{+0.04}_{-0.05}$	$2.85^{+0.03}_{-0.08}$	10	$0.01^{+0.17}$	$0^{+0.3}$	480^{+170}_{-170}	10.1
14	$1.86^{+0.04}_{-0.07}$	$10.6^{+0.6}_{-0.6}$	$6.45^{+0.13}_{-0.05}$	$0^{+0.5}$	$0.11^{+0.06}_{-0.04}$	$2.56^{+0.05}_{-0.06}$	9^{+15}_{-5}	$0.6^{+4}_{-0.3}$	2	50^{+100}_{-50}	7.59
15	$1.48^{+0.05}_{-0.06}$	$15.7^{+1.3}_{-0.8}$	$6.48^{+0.15}_{-0.0.8}$	$0.5^{+0.3}_{-0.3}$	$0.20^{+0.08}_{-0.07}$	$2.23^{+0.05}_{-0.04}$	4.9^{+14}_{-1}	$3.2^{+5}_{-2.4}$	2	100^{+200}_{-100}	7.15
16	$1.42^{+0.03}_{-0.06}$	$17.0^{+1.8}_{-1.4}$	$6.52^{+0.19}_{-0.12}$	$0.65^{+0.15}_{-0.3}$	$0.20^{+0.08}_{-0.07}$	$2.31^{+0.03}_{-0.03}$	$5.4^{+0.7}_{-0.5}$	$2.7^{+1.5}_{-0.1}$	$1.20^{+0.4}_{-0.2}$	600^{+90}_{-90}	8.54
17	$2.15^{+0.03}_{-0.08}$	$11.7^{+1.0}_{-0.5}$	$6.40^{+0.26}$	$0^{+0.5}$	$0.18^{+0.08}_{-0.12}$	$2.82^{+0.05}_{-0.07}$	10	$0.01^{+0.19}$	2	0^{+100}	11.1
18	$1.70^{+0.07}_{-0.06}$	$15.5^{+1.1}_{-1.1}$	$6.48^{+0.16}_{-0.0.8}$	$0.3^{+0.3}_{-0.3}$	$0.24^{+0.11}_{-0.08}$	$2.40^{+0.11}_{-0.07}$	3.6^{+9}_{-1}	5^{+7}_{-3}	2	190^{+140}_{-140}	10.4
19	$1.53^{+0.05}_{-0.07}$	$18.6^{+2.0}_{-0.9}$	$6.51^{+0.15}_{-0.11}$	$0.5^{+0.3}_{-0.3}$	$0.26^{+0.14}_{-0.08}$	$2.30^{+0.18}_{-0.03}$	$4.3^{+6}_{-1.2}$	$4.8^{+1.4}_{-3}$	2	390^{+150}_{-130}	10.5
20	$1.34^{+0.13}_{-0.12}$	24^{+4}_{-4}	$6.42^{+0.25}_{-0.02}$	$0.8_{-0.4}$	$0.41^{+0.14}_{-0.19}$	$2.11^{+0.16}_{-0.17}$	$3.7^{+0.7}_{-0.3}$	$6.2^{+1.5}_{-2}$	$1.7^{+0.5}_{-0.4}$	720^{+120}_{-90}	13.8
21	$1.23^{+0.22}_{-0.12}$	30^{+6}_{-9}	$6.42^{+0.25}_{-0.02}$	$0.8_{-0.4}$	$0.52^{+0.16}_{-0.29}$	$1.95^{+0.37}_{-0.18}$	$3.2^{+0.5}_{-0.2}$	$9.9^{+1.9}_{-3}$	$2.2^{+0.4}_{-0.4}$	1540^{+160}_{-180}	21.8
22	$2.20^{+0.13}_{-0.13}$	$11^{+1.0}_{-1.0}$	$6.40^{+0.3}$	$0^{+0.5}$	$0.20^{+0.12}_{-0.04}$	$2.90^{+0.22}_{-0.14}$	11^{+20}_{-8}	$0.14^{+23}_{-0.13}$	2	100^{+200}_{-100}	14.0
23	$1.56^{+0.14}_{-0.12}$	$17.2^{+1.3}_{-1.2}$	$6.43^{+0.19}_{-0.03}$	$0.75^{+0.05}_{-0.4}$	$0.45^{+0.14}_{-0.19}$	$2.30^{+0.17}_{-0.13}$	$4.0^{+1.3}_{-0.4}$	$5.0^{+1.2}_{-2.2}$	2	120^{+100}_{-100}	9.8
24	$1.30^{+0.06}_{-0.07}$	24^{+10}_{-4}	$6.49^{+0.20}_{-0.09}$	$0.68^{+0.12}_{-0.3}$	$0.30^{+0.14}_{-0.11}$	$2.00^{+0.2}_{-0.2}$	$3.7^{+0.7}_{-0.4}$	$6.3^{+0.9}_{-0.4}$	2	500^{+220}_{-200}	13.2
25	$1.48^{+0.07}_{-0.07}$	$19.4^{+2.1}_{-1.8}$	$6.54^{+0.24}_{-0.14}$	$0.65^{+0.15}_{-0.4}$	$0.26^{+0.15}_{-0.11}$	$2.42^{+0.03}_{-0.10}$	$5.2^{+1.6}_{-1.1}$	$3.5^{+2.1}_{-2.6}$	$1.6^{+0.4}_{-0.7}$	940^{+110}_{-140}	16.5
26	$2.29^{+0.12}_{-0.15}$	$11.2^{+1.0}_{-0.7}$	$6.46^{+0.21}_{-0.06}$	$0.24^{+0.3}_{-0.24}$	$0.27^{+0.12}_{-0.10}$	$2.94^{+0.14}_{-0.18}$	11^{+9}_{-7}	$0.06^{+8}_{-0.05}$	$0^{+0.5}$	1400^{+300}_{-300}	16.3
27	$2.02^{+0.08}_{-0.04}$	$11.7^{+0.5}_{-0.3}$	$6.54^{+0.10}_{-0.14}$	$0.48^{+0.3}_{-0.5}$	$0.29^{+0.16}_{-0.11}$	$2.82^{+0.03}_{-0.06}$	8^{+3}_{-3}	$0.6^{+3.4}_{-0.5}$	$1.8^{+0.9}_{-0.7}$	540^{+150}_{-140}	10.7
28	$1.60^{+0.04}_{-0.05}$	$14.6^{+1.0}_{-1.0}$	$6.50^{+0.13}_{-0.10}$	$0.61^{+0.19}_{-0.2}$	$0.29^{+0.10}_{-0.07}$	$2.30^{+0.04}_{-0.03}$	17^{+13}_{-10}	$0.06^{+0.6}_{-0.05}$	$0.5^{+1.0}_{-0.5}$	250^{+80}_{-80}	8.2
29	$1.44^{+0.05}_{-0.04}$	$17.1^{+1.0}_{-1.0}$	$6.50^{+0.13}_{-0.10}$	$0.68^{+0.12}_{-0.2}$	$0.26^{+0.08}_{-0.07}$	$2.25^{+0.03}_{-0.03}$	$4.2^{+2.2}_{-0.8}$	4.5^{+3}_{-3}	2	240^{+220}_{-100}	8.5
30	$1.45^{+0.07}_{-0.06}$	$17.0^{+1.6}_{-1.6}$	$6.49^{+0.09}_{-0.09}$	$0.80_{-0.3}$	$0.28^{+0.07}_{-0.11}$	$2.33^{+0.05}_{-0.04}$	$5.7^{+2.8}_{-1.7}$	$2.4^{+2.8}_{-1.7}$	2	270^{+240}_{-50}	9.6
31	$1.46^{+0.08}_{-0.19}$	$18.5^{+6}_{-2.0}$	$6.52^{+0.21}_{-0.12}$	$0.5^{+0.3}_{-0.5}$	$0.25^{+0.10}_{-0.07}$	$2.34^{+0.11}_{-0.3}$	$3.7^{+1.2}_{-0.6}$	$6.0^{+0.4}_{-2.0}$	$1.5^{+0.6}_{-0.5}$	1150^{+110}_{-130}	13.6
32	$2.09^{+0.04}_{-0.09}$	$10.7^{+1.0}_{-0.7}$	$6.40^{+0.29}$	$0.3^{+0.5}_{-0.3}$	$0.22^{+0.18}_{-0.12}$	$2.84^{+0.09}_{-0.10}$	10	$0.11^{+2.4}_{-0.10}$	$0.5^{+1.0}_{-0.5}$	600^{+300}_{-300}	16.1
33	$1.79^{+0.08}_{-0.08}$	$12.7^{+1.6}_{-1.4}$	$6.40^{+0.24}$	$0.4^{+0.4}_{-0.4}$	$0.23^{+0.17}_{-0.10}$	$2.5^{+0.1}_{-0.6}$	$4.1^{+1.4}_{-1.8}$	$3.9^{+4}_{-1.7}$	$0.8^{+0.7}_{-0.8}$	300^{+100}_{-80}	8.7
34	$1.47^{+0.07}_{-0.07}$	$18.5^{+3.5}_{-3}$	$6.40^{+0.27}$	$0.68^{+0.12}_{-0.5}$	$0.20^{+0.11}_{-0.10}$	$2.2^{+0.2}_{-0.5}$	$3.4^{+13}_{-0.5}$	7^{+2}_{-4}	2	300^{+180}_{-180}	8.3
35	$1.40^{+0.09}_{-0.07}$	$19.3^{+2.3}_{-2.7}$	$6.40^{+0.24}$	$0.62^{+0.18}_{-0.4}$	$0.22^{+0.13}_{-0.09}$	$2.31^{+0.07}_{-0.16}$	$5.1^{+25}_{-1.5}$	$3.0^{+2.0}_{-2.2}$	2	100^{+200}_{-100}	10.3
36	$1.46^{+0.07}_{-0.06}$	$16.8^{+1.2}_{-1.8}$	$6.40^{+0.3}$	$0.8_{-0.4}$	$0.29^{+0.09}_{-0.14}$	$2.38^{+0.9}_{-0.18}$	$4.1^{+2.7}_{-0.7}$	$4.6^{+1.8}_{-3}$	$1.9^{+0.7}_{-0.6}$	450^{+90}_{-90}	10.1
37	$2.10^{+0.14}_{-0.12}$	$11.1^{+0.9}_{-0.1}$	$6.47^{+0.26}_{-0.07}$	$0.6^{+0.2}_{-0.6}$	$0.28^{+0.17}_{-0.13}$	$2.83^{+0.4}_{-0.01}$	10	$0.01^{+0.4}_{-0}$	2	100^{+60}_{-60}	6.7
38	$1.71^{+0.08}_{-0.09}$	$13.9^{+0.9}_{-1.0}$	$6.40^{+0.22}$	$0.8_{-0.2}$	$0.38^{+0.12}_{-0.13}$	$2.44^{+0.16}_{-0.15}$	10	$0.4^{+0.3}_{-0.39}$	2	250^{+100}_{-150}	7.4
39	$1.45^{+0.06}_{-0.06}$	$18.8^{+1.9}_{-1.6}$	$6.40^{+0.20}$	$0.8_{-0.2}$	$0.40^{+0.08}_{-0.12}$	$2.23^{+0.10}_{-0.08}$	11^{+30}_{-3}	$0.6^{+1.7}_{-0.6}$	2	100^{+100}_{-100}	8.6
40	$1.42^{+0.06}_{-0.06}$	$19.6^{+2.0}_{-2.6}$	$6.42^{+0.21}_{-0.02}$	$0.8_{-0.2}$	$0.35^{+0.10}_{-0.10}$	$2.22^{+0.10}_{-0.10}$	10^{+20}_{-5}	$0.8^{+2.2}_{-0.8}$	2	90^{+60}_{-60}	9.7
41	$1.51^{+0.06}_{-0.05}$	$17.2^{+1.4}_{-1.4}$	$6.44^{+0.23}_{-0.04}$	$0.8_{-0.2}$	$0.33^{+0.07}_{-0.13}$	$2.34^{+0.06}_{-0.05}$	11^{+13}_{-8}	$0.4^{+2.5}_{-0.4}$	2	170^{+50}_{-50}	9.6
42	1.47	19	$6.47^{+0.28}_{-0.07}$	$0.8_{-0.4}$	$0.28^{+0.05}_{-0.10}$	$2.36^{+0.04}_{-0.04}$	$4.6^{+1.8}_{-1.2}$	$3.4^{+3}_{-2.2}$	$2.5^{+0.7}_{-0.5}$	400^{+160}_{-60}	11.8
43	1.36	22	$6.40^{+0.24}$	$0.8_{-0.14}$	$0.40^{+0.13}_{-0.10}$	$2.25^{+0.04}_{-0.04}$	$4.5^{+1.6}_{-0.6}$	$4.2^{+0.6}_{-2.5}$	$2.0^{+0.7}_{-0.8}$	650^{+60}_{-180}	14.6

Notes.—Parameter values and associated errors for all the CD-resolved spectra adopting the `dbbtt` or the `dbbttpeg` model. The column F_{PEG} gives the power-law flux in units of 10^{-12} ergs cm^{-2} s^{-1} calculated in the 20–200 keV energy range. The column F_{TT} gives the flux of the thermal Comptonization component in units of 10^{-8} ergs cm^{-2} s^{-1} in the 0.1–200 keV energy range. See § 4 for an explanation of the parameters involved in the fits. All the uncertainties are calculated at 90% confidence level.

two tracks mostly overlap. For this reason a HB spectrum, for this analysis, is to be considered only as a simple label for a spectrum extracted from the top part of left track of each CD.

6. THE HOT COMPTONIZATION MODEL

6.1. *Energetics*

In the following we discuss the fit results based on the adopted model `dbbttpeg`. Although in some spectra this model overparameterizes the fit, the spectral behavior of the source and our conclusions would not change, if we used the best-fitting values of the `dbbtt` modelization (we show in Table 3 the best-fit values of the spectral parameter, together with associated errors quoted at 90% confidence level). In some cases we had to freeze some parameters in order to make the fit physically consistent and avoid solutions without physical meaning. In spectra 7, 8, 12, 13, 17, 37, and 38 the electron temperature had to be fixed to 10 keV (a value consistent with what we found in other CDs for the same CD zone; if free, the fit would give a best-fit with $kT_0 > kT_e$, which is clearly wrong), the photon index of the `pegpwrlw` component in spectra where this component is not significantly detected, or when its value is unconstrained by the fit, is frozen to a reference value of 2; the `diskbb` parameters of spectra 42 and 43 had to be fixed to the best values as obtained by the best-fit model `dbbtt` (if free, this component vanishes, while the `comptt` and `pegpwrlw` have comparable flux values).

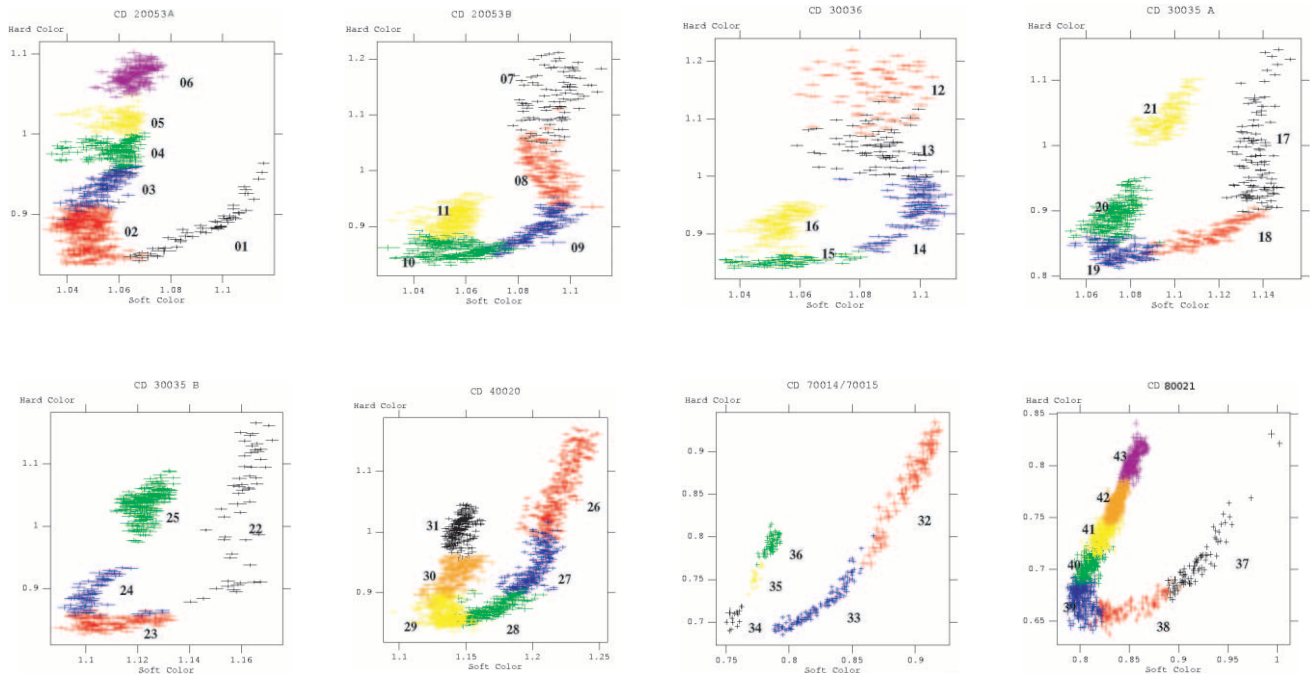

FIG. 1.—CDs extracted from *RXTE* data sets used in our spectral analysis. Different colors indicate different selected regions from which the CD-resolved spectra were produced. We label the spectra through a progressive numbering, as shown in the CDs.

In this spectral decomposition we calculated the total luminosity as follows:

$$L_{\rm X} = 4\pi D^2 \left(F_{\rm TT} + F_{\rm PEG} + a\xi N_{\rm DB} T_{\rm DB}^4\right), \qquad (1)$$

where $F_{\rm TT}$ is the `comptt` flux and $F_{\rm PEG}$ is the `pegpwrlw` flux extrapolated in the 0.1–200 keV energy range; $\xi = 1/(f^4\kappa^2)$, where f is the spectral hardening factor (Shimura & Takahara 1995), is assumed equal to 1.7, and $\kappa \sim 0.4$ corrects for the fact that the radius at which is reached the maximum temperature is greater than the inner disk distance (Vierdayanti et al. 2006). The value a is a constant dependent on the distance of the source, which we assumed to be 2.8 kpc, and the inclination of the disk, which we assumed to be 45°. In Figure 1 we show the contribution of the disk and of the Comptonized component to the total flux. The luminosities on both axes are in Eddington units for a 1.4 $M_\odot$.

The source spans a luminosity range between $0.9L_{\rm Edd}$ and $2.4L_{\rm Edd}$, thus being in a super-Eddington state almost independently of the position of the source on the CD. We note that the only way to drastically reduce this range is to suppose a very massive compact object (the possibility of a massive NS hosted in the Sco X-1 system is also discussed in Stella & Vietri [1999] in the framework of the relativistic precession model used to explain the frequencies of quasi-periodic oscillations in NSs and BH systems) given that both the distance and the inclination angle are known with good accuracy (10% and 13% relative error, respectively).

The disk flux and the hard flux correlate as expected with the total flux, although the disk emission presents a more pronounced linear relation, while the hard flux seems to saturate as the total flux reaches the highest values. If we assume a linear dependency of the two contributions versus the total emission we derive a constant of proportionality equals to 0.56 for the disk flux and 0.44 for the Comptonized flux. When we look at the ratio of

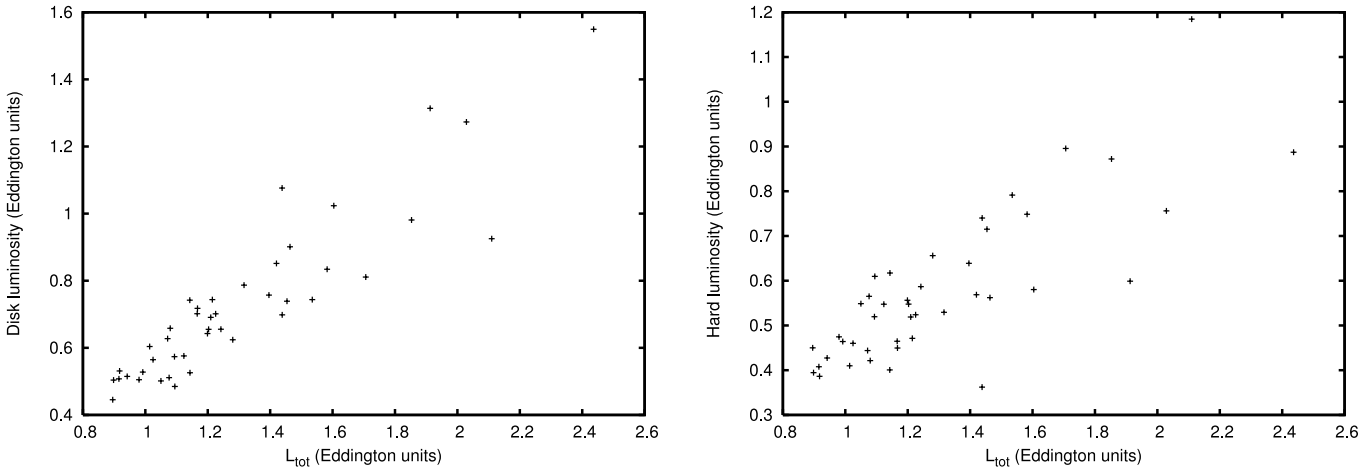

FIG. 2.—*Left*: Soft (disk) luminosity for the extracted spectra vs. total (0.1–200 keV) luminosity. *Right*: Hard (Comptonized) luminosity for the extracted spectra vs. total (0.1–200 keV) luminosity. All luminosities are in Eddington units for a 1.4 $M_\odot$ NS. [*See the electronic edition of the Journal for a color version of this figure.*]

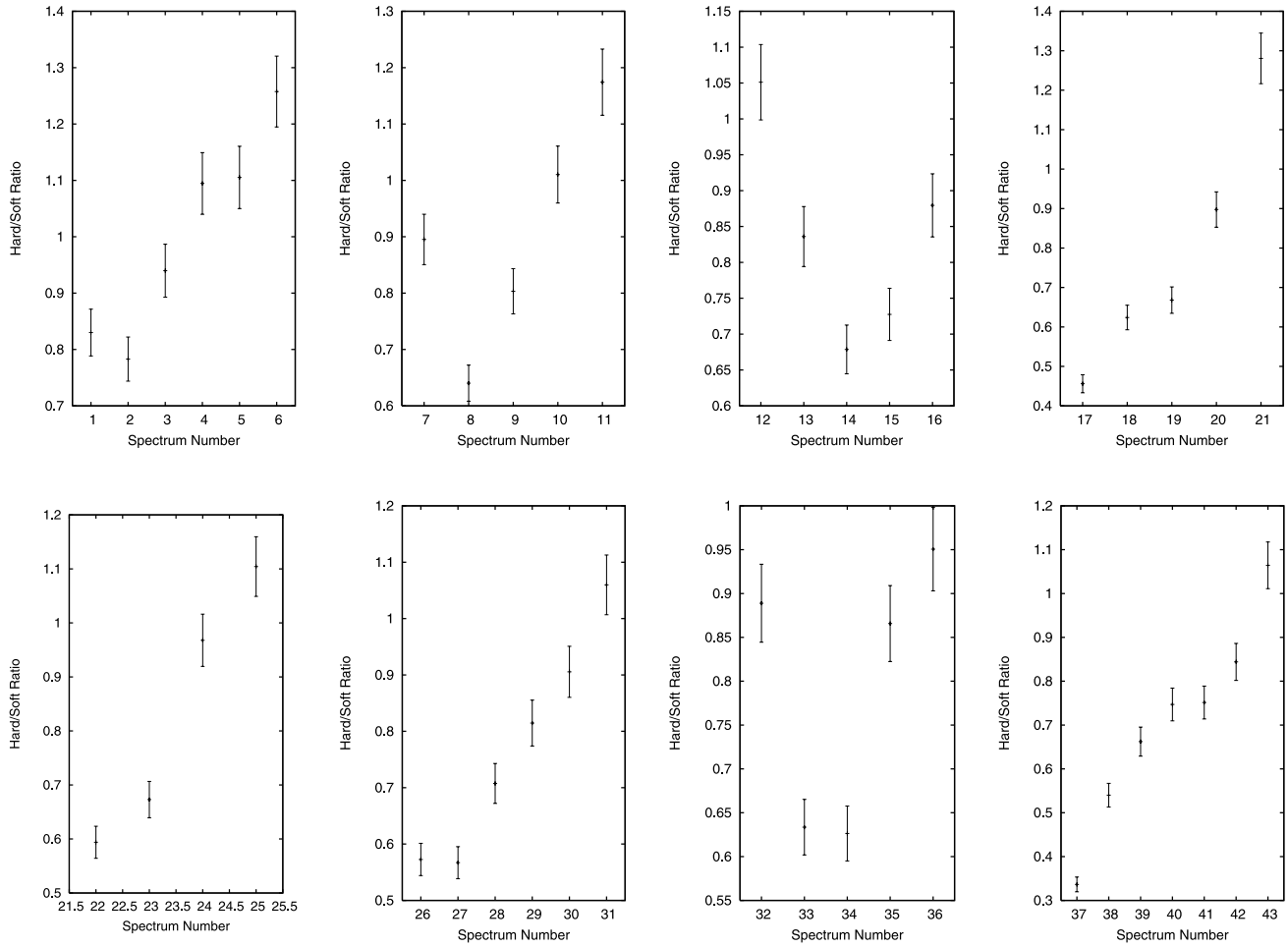

FIG. 3.—Ratio of the hard/soft luminosities for all the CD-extracted spectra. In the *x*-axis the number refers to the spectrum, as indicted in Table 2. We assumed a 5% error for the ratio of the two fluxes. [*See the electronic edition of the Journal for a color version of this figure.*]

the two contributions along the *Z* track (see Fig. 2; a 5% error on this ratio is assumed, after having tested the corresponding hard and soft flux values for different parameter values of the spectral components inside the uncertainty error bars as derived from the fits), there is a general trend to have a higher hard/soft ratio as the source moves from higher to lower accretion states; this is in agreement with our expectation that, at lower accretion rate, the disk could be truncated and the fraction of the power dissipated in the boundary layer should correspondingly increase. Spectra 7, 12, 13, and 32 do not follow this trend; these spectra belong to the topFB spectra, and in these cases, we are possibly underestimating the disk contribution, or overestimating the hard flux.

6.2. *Disk Emission and Thermal Comptonization*

We present in Figure 3 the dependency of the inner disk radius and of the inner disk temperature, plotted against the hard/soft

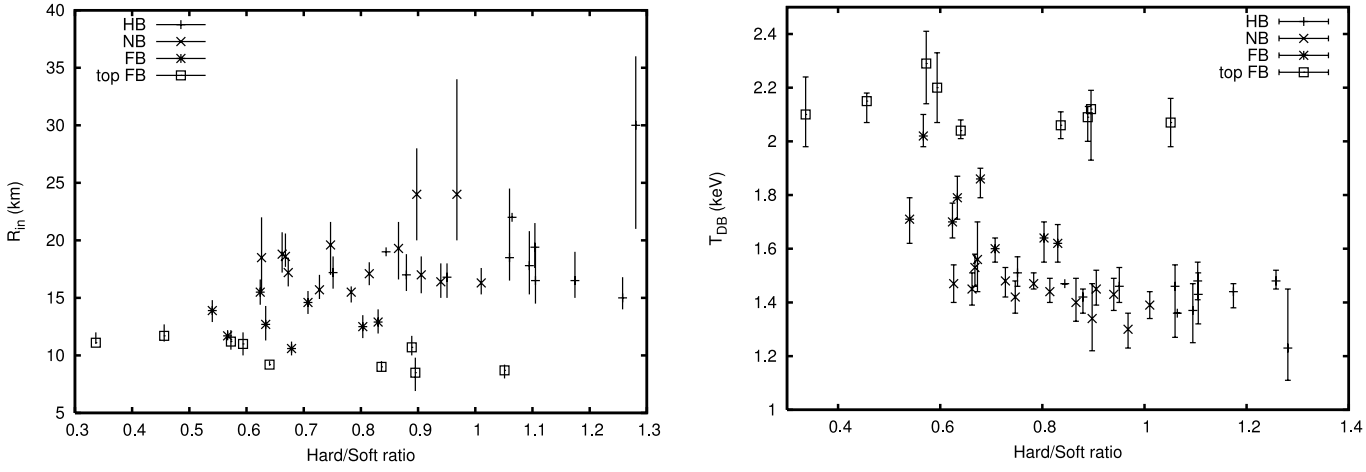

FIG. 4.—*Left*: Inner disk radius vs. the hard/soft ratio. *Right*: Temperature at the inner disk radius vs. the hard/soft ratio. [*See the electronic edition of the Journal for a color version of this figure.*]

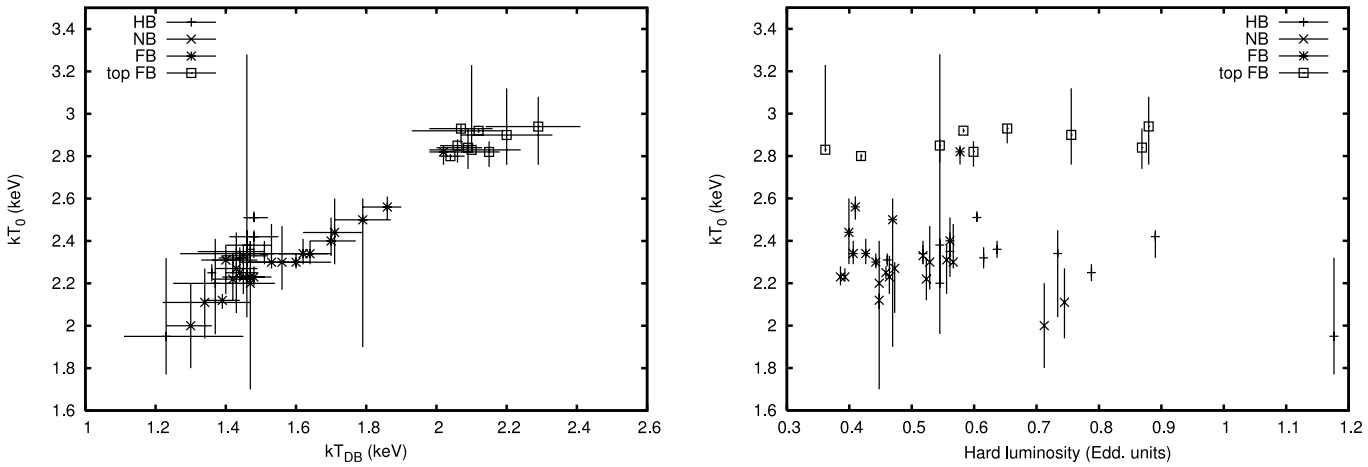

FIG. 5.—*Left*: Soft seed photon temperature kT_0 vs. the inner disk temperature kT_{DB}. *Right*: Soft seed photon temperature kT_0 vs. hard (`comptt` + `pegpwrlw`) luminosity. [*See the electronic edition of the Journal for a color version of this figure.*]

luminosity ratio. It is shown, both in Table 3 and in Figure 4, the apparent radius, derived without considering important correction factors, due to the color/effective temperature ratio, relativistic effects, and the nonzero torque boundary conditions; moreover, it should be noted that these corrective factors can also vary, depending on the accretion state. The sum of all these effects could be a drastic rescale of the measured inner radii up to almost an order of magnitude higher (Merloni et al. 2000), but the general trend that correlates this parameter with the accretion state of the source should be qualitatively preserved.

The apparent inner disk radius, for spectra in the topFB, has the lowest values, $\leq$10 km, while the average value for NB spectra and HB spectra is considerably higher (average value: $\sim$18 km for the HB and NB, $\sim$13.5 km for the FB, and $\sim$10.2 km for the topFB). The inner disk temperature, on the other hand, presents the highest values, as one could expect, on the FB, while the temperature diminishes with the accretion rate. A small subset of FB spectra falls out of the trend, but as pointed out earlier, in this case, the exact determination of the relative contributions of the two components could suffer as a result of systematic uncertainties linked to the particularly luminous state of the source. On the FB the disk temperature has an average value of 2.12 keV, while on the lower part of the FB it sinks to 1.73 keV. There is not any appreciable difference on temperature for spectra taken on the NB and on the HB with an average value of 1.43 keV.

For the hard, thermal Comptonized component the accurate determination of all the spectral parameters was not always possible. The soft seed photon temperature presents, for each spectra analyzed, a substantially higher value with respect to the disk temperature at the inner radius. We hence propose that the soft photons are originated from the boundary layer/NS surface, partially thermalized with the softer photons of inner part of the accretion disk around the NS. Moreover, calculating the radius of the soft seed photon emitting region R_w from

$$R_w = 3 \times 10^4 \, d \sqrt{\frac{f_{\rm bol}}{1+y}} \Big/ (kT_0)^2, \qquad (2)$$

where d is the distance to the source in kiloparsecs, $f_{\rm bol}$ is the `comptt` bolometric flux, and y (see eq. [3]) is the Compton parameter, we derived for our sample values in the 3–6 km range that clearly indicate a rather small emitting region, thus supporting our identification.

The CD-correlated changing of the thermal temperatures is compatible with a scenario in which the position of the source on the CD is determined by the instantaneous $\dot{M}$, and higher accretion rates correspond to higher seed photon temperatures, resulting in a hotter radiation field. The soft seed photon temperature has 2.2, 2.4, and 2.9 keV average values for spectra on the HB/NB, FB, and topFB, respectively. When plotted against each other, the disk temperature and the soft seed photon temperature (see Fig. 5, *left*) follow each other quite closely, as these two parameters are the main driving physical quantities related to the accretion state of the source. The correlation between the CD-resolved spectra and the two temperatures shows, although in a qualitative representation, that the link between the spectral evolution of the source and its accretion state is well motivated.

The other two spectral parameters, which describe the high-energy curvature of the Comptonized component, the electron temperature of the Comptonizing plasma (kT_e), and the optical depth of the cloud τ, are not always well constrained by the fit. As is evident from Figure 6, for spectra at high accretion rate we obtained high values for the electron temperature ($kT_e \geq 10$ keV) and low values for the optical depth ($\tau \leq 1$). As the source resides on zones of lower $\dot{M}$, the Comptonizing cloud substantially thickens, while the electron temperature correspondingly diminishes. Plotting the subset of the spectra in the NB and HB helps to better visualize this tendency (Fig. 6, *right*). It is to be noted that the determination of these two parameters is partially related with the hard power-law component; although there are spectra where the `pegpwrlw` component is not strictly necessary for a good fit, its introduction slightly shifts the thermal Comptonized component to lower energies, thus giving a noticeable reduction in the uncertainties of the Compton curvature.

In all the spectra a Gaussian line at energies $\sim$6.4 keV is required. It mostly appears rather broad, with a line width that often reaches our constraint of 0.8 keV. The equivalent widths associated with the line are in the 80–200 eV range, and are to be taken as rather indicative given the low-energy resolution of the PCA and the presence of systematic residuals in this energy range.

6.3. *The Hard Tail Behavior*

The presence of a hard X-ray excess in the extracted spectra of Sco X-1 is mostly evident in 18 spectra from a total of 43 CD-selected spectra. There is little evidence of the presence of hard X-ray excess for spectra lying in the bottom part of the FB and of

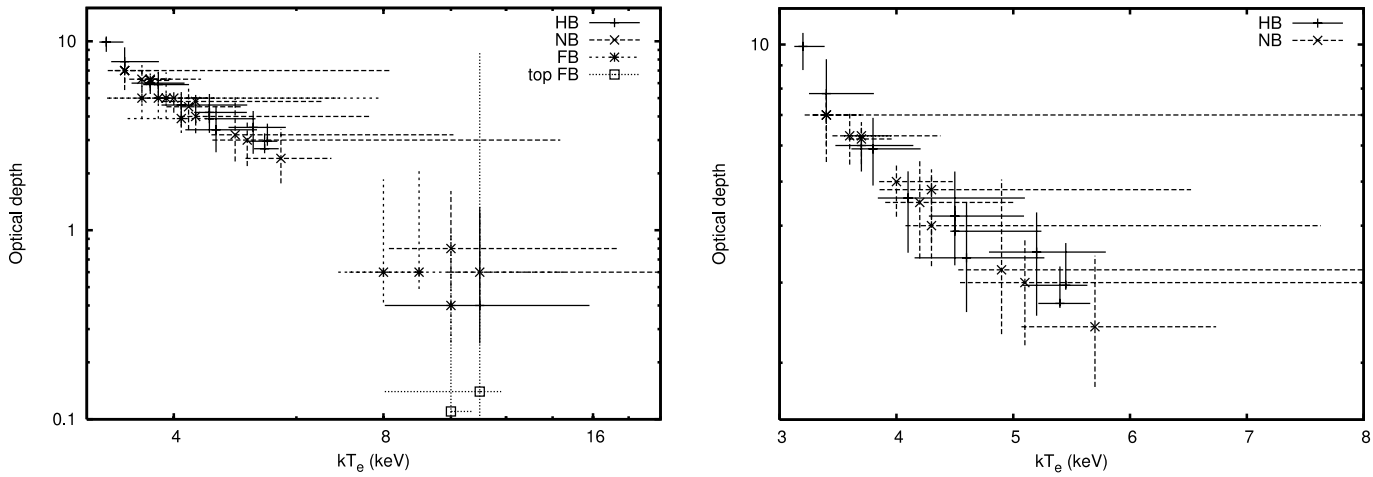

FIG. 6.—*Left*: Optical depth vs. electron temperature (all spectra). *Right*: Optical depth vs. electron temperature (subset of spectra on the HB/NB). Error bars show 1.0 σ errors. [*See the electronic edition of the Journal for a color version of this figure.*]

the NB, namely for spectra taken near the apex that connects the left and right track that compose the *V* pattern.

In all the examined CD patterns we always detect a power-law high-energy excess, dominant above ~40 keV, as the source resides at the top of the left track, i.e., a portion of the diagram that we tentatively identified with the HB, and that should correspond to the lowest mass accretion rate. This group of spectra are characterized by the lowest values of inner disk temperature and soft seed photon temperature; the derived inner disk radii correspond to a disk truncated at about $10R_g$–$15R_g$, while the Comptonizing optical cloud is substantially thicker with respect to any other spectrum in other zones of the CD; the fraction of the total power dissipated in the Comptonizing corona has the highest values, with a ratio hard/soft luminosity well above unity.

Apart from this consistent group of HB/NB spectra, we also found a minor group of spectra (namely five spectra: 7, 8, 12, 13, and 26), for which the fit required a third high-energy component. These spectra belong to three CDs (20035B, 30036, and 40020) and are spectra taken at the top of the FB. Although these spectra are located in the same CD region, not all the CDs that display a topFB clearly show this excess. This could be due to a statistical reason, as in all the other CDs the HEXTE count rate (see Table 2) drops of about 1 order of magnitude with respect to these three CDs; because the count rate is essentially concentrated in the 20–35 keV energy band, which is the range that constrains the curvature of the thermal Comptonized component, the energy channels in this energy band with a high statistic will drive the fit, and any small excess above the exponential tail of the Comptonized component will statistically be more accentuated. However, we cannot exclude that an opposite reasoning is true, i.e., that we are underestimating instrumental effects that appear only for higher count rates as dead-time corrections or poor background estimate, so that these particular hard tails are artifacts of an incorrect modelization of the thermal Comptonization curvature. As we have no apparent way to better calibrate our spectra, we also discuss the appearance of this component for this group of spectra. Future observations with other high-energy satellites, such as *INTEGRAL* or *Suzaku*, will test whether this particular topFB state of the source is also accompanied by a high-energy excess, or whether it is an HEXTE faked detection.

The hard excess has no evident relation with the total luminosity of the source, but this could be expected, since the different zones of the CD track are not related with the total X-ray luminosity. Using the pegged power law, we directly derived from the

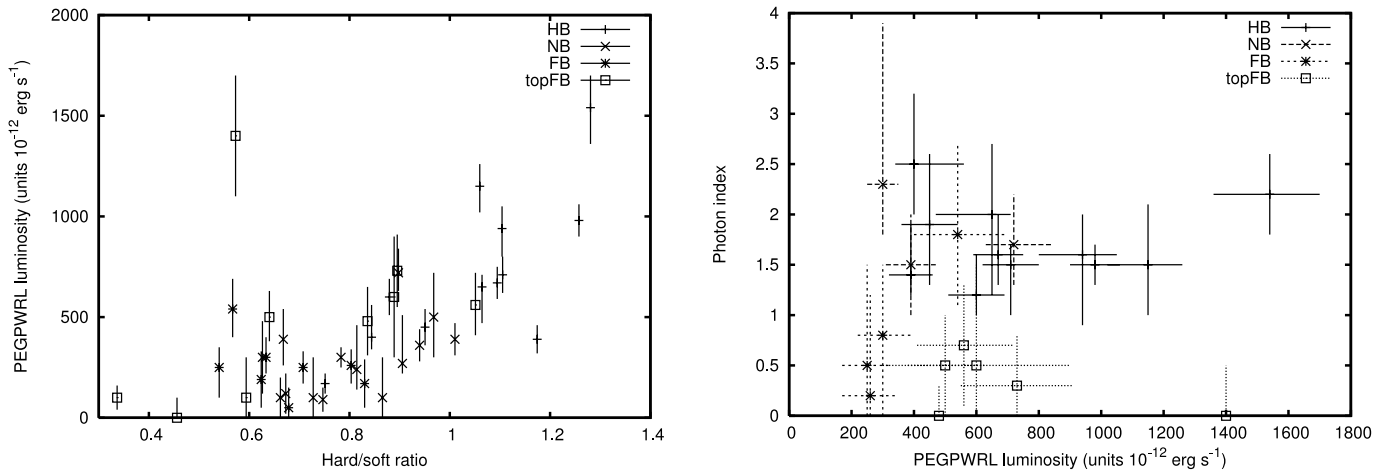

FIG. 7.—*Left*: Hard tail luminosity (in the 20–200 keV energy range) vs. the hard/soft ratio. *Right*: Energy index of the `pegpwrlw` component vs. its 20–200 keV luminosity (the subset of spectra for which the photon index was not constrained by the fit is excluded from this figure). [*See the electronic edition of the Journal for a color version of this figure.*]

TABLE 4
FIT RESULTS: THE HYBRID COMPTONIZATION MODEL

Parameter	kT_{DB} (keV)	R_{in} (K) (km)	Line E (keV)	σ (keV)	N_{Gaus} (photons cm^{-2} s^{-1})	l_h	kT_{BB} (keV)	l_{nth}/l_h	τ_p	G_{inj}	$Flux_{eqp}$
02.....	$1.42^{+0.02}_{-0.04}$	16^{+7}_{-4}	$6.50^{+0.13}_{-0.1}$	$0.58^{+0.22}_{-0.23}$	$0.18^{+0.05}_{-0.04}$	$0.65^{+0.03}_{-0.04}$	$2.20^{+0.07}_{-0.08}$	38^{+9}_{-5}	$0.81^{+1.07}_{-0.13}$	2	8.59
04.....	$1.31^{+0.05}_{-0.04}$	19^{+8}_{-7}	$6.45^{+0.25}_{-0.05}$	$0.8_{-0.5}$	$0.26^{+0.04}_{-0.15}$	$0.98^{+0.09}_{-0.26}$	$2.21^{+0.06}_{-0.06}$	62^{+3}_{-4}	$1.7^{+0.7}_{-0.7}$	2	11.52
05.....	$1.30^{+0.06}_{-0.03}$	19^{+8}_{-9}	$6.50^{+0.20}_{-0.1}$	$0.8_{-0.4}$	$0.22^{+0.06}_{-0.1}$	$1.01^{+0.13}_{-0.17}$	$2.24^{+0.05}_{-0.07}$	63^{+3}_{-4}	$1.8^{+0.3}_{-0.7}$	2	12.33
06.....	$1.44^{+0.04}_{-0.12}$	16^{+10}_{-6}	$6.50^{+0.20}_{-0.1}$	$0.46^{+0.09}_{-0.11}$	$0.12^{+0.04}_{-0.04}$	$0.88^{+0.14}_{-0.05}$	$2.46^{+0.03}_{-0.08}$	73^{+2}_{-4}	$0.64^{+0.6}_{-0.09}$	2	12.46
11.....	$1.48^{+0.06}_{-0.14}$	18^{+13}_{-6}	$6.40^{+0.16}$	$0.6^{+0.2}_{-0.3}$	$0.25^{+0.11}_{-0.07}$	$1.12^{+0.10}_{-0.10}$	$2.17^{+0.07}_{-0.14}$	53^{+11}_{-6}	$2.81^{+0.14}_{-0.16}$	2	13.25
16.....	$1.16^{+0.05}_{-0.02}$	25^{+12}_{-10}	$6.40^{+0.20}$	$0.8_{-0.3}$	$0.38^{+0.03}_{-0.07}$	$2.02^{+0.17}_{-0.04}$	$1.93^{+0.036}_{-0.13}$	75^{+7}_{-3}	$7.3^{+0.3}_{-0.3}$	2	11.39
20.....	$1.36^{+0.05}_{-0.05}$	23^{+8}_{-7}	$6.50^{+0.20}_{-0.1}$	$0.6^{+0.2}_{-0.2}$	$0.31^{+0.2}_{-0.09}$	$1.32^{+0.3}_{-0.5}$	$2.06^{+0.07}_{-0.07}$	54^{+3}_{-1}	$4.0^{+0.8}_{-3}$	2	14.99
21.....	$1.24^{+0.04}_{-0.05}$	28^{+10}_{-14}	$6.46^{+0.19}_{-0.06}$	$0.8_{-0.4}$	$0.43^{+0.13}_{-0.13}$	$1.29^{+0.06}_{-0.17}$	$2.12^{+0.1}_{-0.02}$	52^{+3}_{-2}	$2.8^{+1.6}_{-0.9}$	2	12.31
25.....	$1.24^{+0.01}_{-0.07}$	26^{+10}_{-6}	$6.42^{+0.18}_{-0.02}$	$0.8_{-0.2}$	$0.41^{+0.06}_{-0.09}$	$1.28^{+0.13}_{-0.18}$	$2.09^{+0.04}_{-0.03}$	47^{+3}_{-2}	$2.8^{+0.6}_{-0.2}$	2	11.14
31.....	$1.31^{+0.11}_{-0.02}$	22^{+8}_{-9}	$6.48^{+0.22}_{-0.08}$	$0.8_{-0.2}$	$0.36^{+0.06}_{-0.14}$	$1.11^{+0.09}_{-0.16}$	$2.20^{+0.17}_{-0.06}$	67^{+8}_{-1}	$1.9^{+0.4}_{-0.7}$	2	16.52
36.....	$1.44^{+0.08}_{-0.09}$	17^{+9}_{-8}	$6.40^{+0.27}$	$0.7^{+0.1}_{-0.5}$	$0.21^{+0.12}_{-0.12}$	$0.62^{+0.2}_{-0.23}$	$2.34^{+0.09}_{-0.11}$	50^{+10}_{-8}	$0.6^{+0.8}_{-0.4}$	2	2.47
42.....	$1.51^{+0.06}_{-0.05}$	11^{+5}_{-3}	$6.40^{+0.3}$	$0.8_{-0.5}$	$0.11^{+0.03}_{-0.05}$	$0.33^{+0.09}_{-0.04}$	$2.40^{+0.07}_{-0.12}$	43^{+7}_{-8}	$0.20^{+0.6}_{-0.15}$	2	12.1
43.....	$1.41^{+0.07}_{-0.04}$	12^{+5}_{-5}	$6.42^{+0.26}_{-0.02}$	$0.8_{-0.3}$	$0.125^{+0.008}_{-0.05}$	$0.64^{+0.11}_{-0.18}$	$2.29^{+0.13}_{-0.06}$	41^{+4}_{-6}	$0.6^{+0.6}_{-0.4}$	2	1.4.3
07.....	$1.95^{+0.02}_{-0.06}$	$1.03^{+0.09}_{-0.06}$	$6.4^{+0.17}$	$0.0^{+0.5}$	$0.09^{+0.021}_{-0.03}$	$0.85^{+0.14}_{-0.21}$	$2.74^{+0.10}_{-0.06}$	100_{-1}	$0.60^{+0.25}_{-0.24}$	$0.9^{+0.8}_{-0.9}$	12.62
08.....	$1.93^{+0.07}_{-0.05}$	$1.17^{+0.05}_{-0.07}$	$6.4^{+0.2}$	$0.0^{+0.5}$	$0.10^{+0.03}_{-0.05}$	$0.89^{+0.08}_{-0.3}$	$2.68^{+0.07}_{-0.03}$	100_{-4}	$0.47^{+0.3}_{-0.5}$	$0.8^{+1}_{-0.8}$	8.62
12.....	$1.98^{+0.06}_{-0.14}$	$1.00^{+0.01}_{-0.01}$	$6.4^{+0.2}$	$0.0^{+0.4}$	$0.09^{+0.03}_{-0.05}$	$0.72^{+0.11}_{-0.3}$	$2.82^{+0.03}_{-0.05}$	100_{-6}	$0.32^{+0.4}_{-0.3}$	$0.2^{+1.7}_{-0.2}$	13.08
13.....	$1.90^{+0.05}_{-0.03}$	$1.20^{+0.05}_{-0.1}$	$6.4^{+0.2}$	$0.0^{+0.5}$	$0.09^{+0.02}_{-0.04}$	$0.65^{+1.0}_{-0.13}$	$2.67^{+0.14}_{-0.02}$	92^{+4}_{-17}	$0.71^{+0.7}_{-0.13}$	$0.86^{+0.54}_{-0.86}$	10.68
26.....	$2.07^{+0.14}_{-0.03}$	$1.97^{+0.08}_{-0.3}$	$6.5^{+0.25}_{-0.1}$	$0.3^{+0.5}_{-0.3}$	$0.30^{+0.2}_{-0.13}$	$1.04^{+0.1}_{-0.5}$	$2.73^{+0.14}_{-0.05}$	100_{-3}	$0.70^{+0.3}_{-0.7}$	$0.0^{+1.6}$	3.023

NOTES.—Parameter values and associated errors, adopting the model `dbbeqpair` for the selected spectra on the HB/NB (first part of the table) and for spectra on the top of the FB (second part of the table). The model for the five FB spectra differs from the one adopted for the HB/NB spectra, as it uses a more appropriate disk emission model (`diskpn`, in XSPEC) instead of the `diskbb` component. For the `diskbb` component we list the derived apparent inner disk radii in kilometers, while for the spectra fitted with the `diskpn` component, the inner disk radius has been fixed to $6R_g$ and the second column shows the value of the normalization of the component in units of $M_\odot^2 \cos(i)/(D^2\beta^4 \times 10^2)$, where the distance is given in kiloparsecs, β is the color/effective temperature, and i is the inclination angle of the disk. The unabsorbed flux of the EQPAIR component has been calculated in the 0.1–200 keV energy range and is in units of 10^{-8} ergs cm^2 s^{-1}. See § 4 for an explanation of all the other parameters involved in the fits. All the uncertainties are calculated at 90% confidence level.

normalization value of this component, the flux in the 20.0–200.0 keV energy band. We show in Figure 7 (*left*) the hard tail luminosities in the 20–200 keV range versus the hard/soft ratio. From the plot it can be clearly seen that the hardening of the spectrum is reflected in the increasing luminosity of the hard tail component; the CD-resolved spectra are, correspondingly, disposed on this plot: the FB spectra reside on the bottom left of the diagram with hard fluxes $\leq 2 \times 10^{-10}$ ergs s^{-1}, NB spectra are harder, and half of them show significant fluxes ($\sim 4 \times 10^{-10}$ ergs s^{-1}), while the HB spectra, in the right part of the plot, show the strongest hard X-ray emission [in the range $(6–12) \times 10^{-10}$ ergs s^{-1}].

As pointed out in the previous section, we found for the topFB sample, spectra with no detectable hard X-ray emission that occupy the left bottom part of this figure and that smoothly join the correlation between hard/soft ratio and hard flux, and spectra that do not follow this trend and for which there is both in the `comptt` and in the `pegpwrlw` component a hard flux higher than we expected. From the figure is also evident that one of the most luminous hard tails is found in a particular spectrum on the topFB (namely spectrum 26 of CD 40020); the luminosity of this component is related to the total broadband high luminous state of the source, which reaches in this case the highest value of total luminosity ($2.6L_{Edd}$) observed in our sample.

On the other hand, the values of the photon index present a well-defined bimodal distribution according to the position of the source on the CD. We find quite flat power laws, with index values

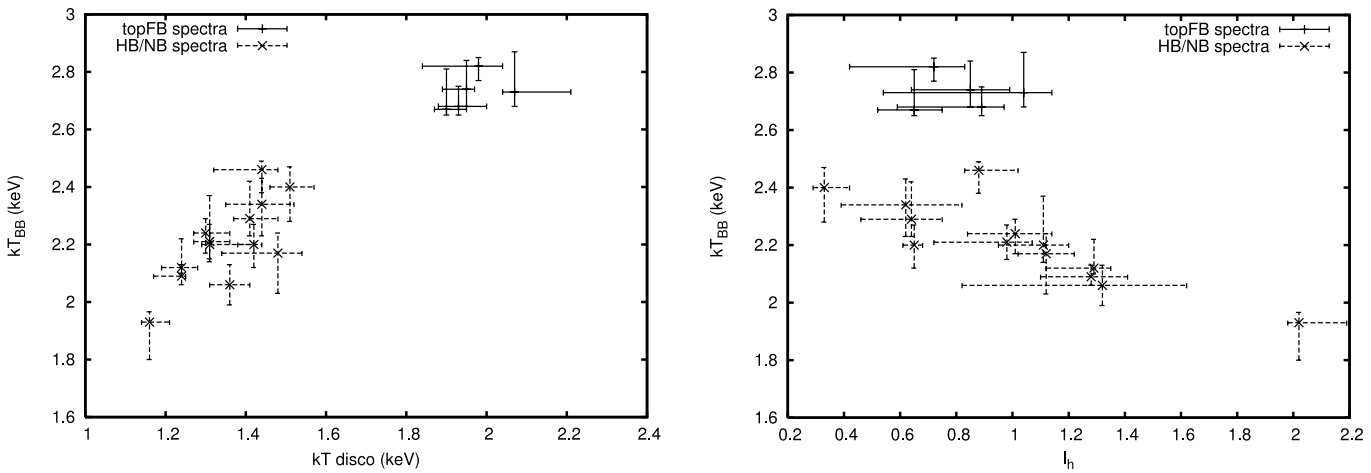

FIG. 8.—*Left*: Soft seed photon temperature kT_{BB} vs. inner disk temperature kT_{disk} (which corresponds to the kT_{DB} value of the `diskbb` component for the HB/NB spectra and to the kT_{max} value of the `diskpn` component for the topFB spectra) for spectra fitted using the `dbbeqpair` modelization. *Right*: Soft seed photon temperature plotted against the hard compactness parameter. [*See the electronic edition of the Journal for a color version of this figure.*]

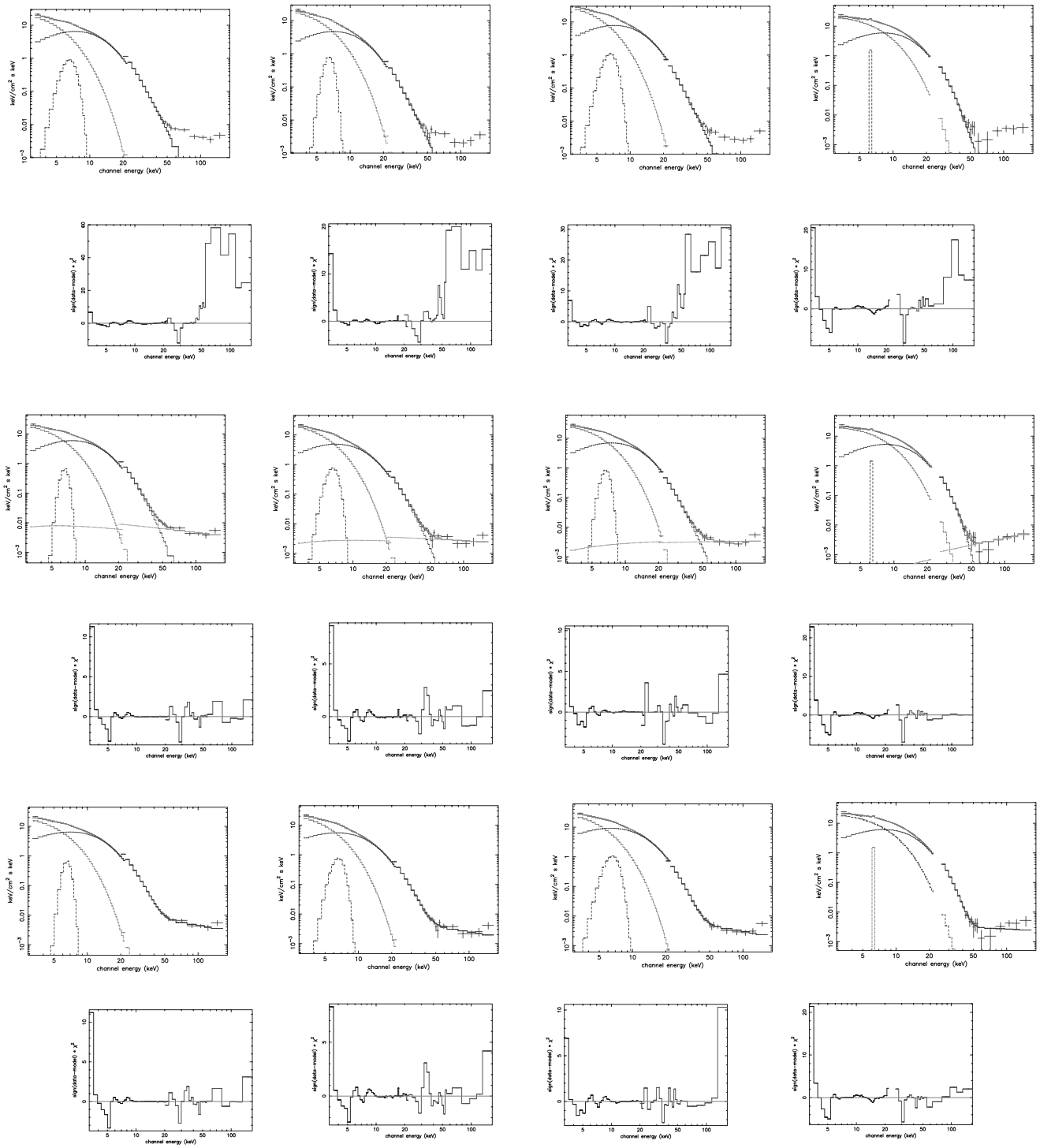

FIG. 9.—Deconvolved spectra, in the $E^*f(E)$ representation, and contributions per channel to the χ^2 for four spectra of our sample. *First column*: Spectrum 06. *Second column*: Spectrum 16. *Third column*: Spectrum 31. *Fourth column*: Spectrum 07. Deconvolved spectra (*upper panels*) and contributions to the χ^2 (*lower panels*) from the best fit using the `dbbtt`, `dbbttpeg`, and `dbbeqpair` models for the top two, middle two, and bottom two rows respectively. [*See the electronic edition of the Journal for a color version of this figure.*]

less than unity for all the FB and topFB spectra, while for the other group of spectra, values generally range between 1.5 and 2 (Fig. 7, *right*).

6.4. *The Hybrid Comptonization Model*

Models of hybrid Comptonization have so far been mostly adopted to explain state transitions both in black hole candidate systems (as in Cyg X-1, Gierliński et al. 1999; GRS 1915+105, Zdziarski et al. 2001; or GX 339+4, Wardziński et al. 2002) and in NS system (GX 17+2; Farinelli et al. 2005).

We tried to model the spectra for which we detected a hard tail, making the hypothesis that both the hard tail and the thermal Comptonized component were related to each other. In this way, all the broadband evolution of the source is covered in a self-consistent way by only two spectral components: the thermal soft disk emission and the hard hybrid Comptonized component.

In Table 4 we present the results of our fits for the group of 18 spectra, distinguishing between the HB/NB group (top part of the table), for which we used the `diskbb` component as in the case of `dbbttpeg` modelization, and the topFB spectra, for which we used the `diskpn` component, under the assumption that for this state the disk is not truncated, and reaches the surface of the NS (we assumed that this happens at a distance of $6R_g$).

As in the case of the previously adopted modelization, the thermal disk temperature and the soft seed photon temperature are the main driving physical parameters that determine the changing of the spectral state of the source. We show in Figure 8 (*left*) the correlation between the two temperatures: the topFB spectra occupy the top right part of the plot, with an average $kT_{\rm BB}$ value of 2.73 keV and inner disk temperature $kT_{\rm DB}$ of 1.97 keV, while the set of the HB-NB spectra are disposed along a linear trend in the 1.2–1.8 keV energy range for the disk temperature and the 1.9–2.5 keV range for the soft seed photon temperature. The plot closely follows the plot of Figure 5 (*right*).

The hard compactness l_h results for all the examined spectra are only a small fraction of the soft compactness l_s, with values of hard/soft ratio l_h/l_s below 0.2. The HB/NB spectra span almost an order of magnitude in the l_h range, while the topFB spectra are all grouped in a more narrow range of values, around $l_h = 0.6$–0.8 (see Fig. 8, *right*).

The two groups of spectra significantly differ both in the τ and $l_{\rm nth}/l_h$ values (it is to be noted, however, that the optical depth reported from the fits has not the same physical meaning of the classical Thomson optical depth of the Comptonizing cloud, as it more properly refers to the optical depth associated with the background photon radiation field): HB spectra present generally higher values of optical depth (with an average value of $\tau_p \sim 2.2$) and a hybrid electron distribution (with $0.3 < l_{\rm nth}/l_h < 0.8$, and an average value of 0.55), while the topFB spectra have considerably lower values of $\tau_p \leq 1$ and essentially nonthermal spectra, with $l_{\rm nth} \simeq 1$. The slope of the high-energy power law of the hybrid electron distribution, $\Gamma_{\rm inj}$, is consistent with a value of 2, for the HB-NB spectra, while for the topFB spectra its value is considerably lower (between 0 and 1).

7. CONCLUSIONS

We outline our main conclusions from an extensive analysis of Sco X-1 *RXTE* observations in the 3–200 keV energy range: we observe a spectral evolution of the source that is clearly dependent on the position of the source along its CD track; the spectral decomposition consists of four different spectral components that we interpret, from the softest to the highest X-rays, respectively, as follows: a soft thermal component from an optically thick accretion disk; a thermal Comptonization from the boundary layer; a reflection component that mainly manifests in a broad Gaussian line at 6.4 keV; and a variable hard excess above 30 keV, mostly present at low $\dot{M}$.

We have shown that the CD-correlated variations of the two thermal temperatures (disk temperature and soft seed photon temperature), the trend in the hard/soft ratio, the Compton thickening of the Comptonizing cloud, and the appearance of significant hard X-ray emission on the HB/NB are the main spectral characteristics of the source.

We paid particular attention to the modelization of the hardest X-ray component, which is of primary importance for the understanding of all the continuum emission, as it has a major impact on the determination of all the other spectral parameters. To fit this hard excess we modeled our spectra using a phenomenological component, i.e., a power law with a low-energy exponential cutoff at the seed photon temperature and a self-consistent physical model, a hybrid thermal/nonthermal Comptonization code. In both cases we found an adequate description of the spectra for each source state, and the two modelizations are statistically equivalent.

The use of simple power laws to fit the hard tails in the *Z*-class sources, but also in some atolls (Tarana et al. 2007; Fiocchi et al. 2006), has been largely used in the past, given the lack of broadband coverage up to the MeV energies, and a poor understanding of the physical origins of this component. Contrary to what has been previously reported (D'Amico et al. 2001), the presence of the hard tail *is* related to the broadband spectral evolution of the source as inferred from the source position on the *Z* track of its CD: the presence and the values of the photon indexes in Sco X-1 are consistent with the results from fits to spectra on the same zone of the CD for the other *Z* sources (Asai et al. 1994; Di Salvo et al. 2000, 2001, 2006); at the same time, the flux contribution to the total energy output of the sources is of the same order and is anticorrelated to the inferred mass accretion rate. This is clearly shown in the case of the CD 20035A, where the hard tail flux monotonically increases as the source moves from the bottom to the top of its NB/HB.

The only difference, between Sco X-1 and the other similar sources, is constituted by rather flat hard tails that we found when the source is at the top of the FB and that has never been observed in other NSs sources; however, while for every CD that we obtained, we systematically found a hard tail as the source was at the top of the left *V* track, the detection on the FB is presumedly dependent on the HEXTE statistics. Past surveys with the use of scintillation counters on board balloons reported the unusual flattening of the spectrum of Sco X-1 above 40 keV (Agrawal et al. 1971), as well as more recent surveys (Manchanda 2006); it would be interesting to definitively assess the existence of such component: from our analysis, we can only conjecture that this component could be a signature, on the FB, of the trespassing of the Eddington limit on the interface between the accretion disk and the board of the boundary layer, followed by a violent expulsion of part of the accreting matter.

Hard tails on the HB could have a thermal origin, as in the case of the thermal Comptonized component that dominates the spectrum at lower energies (less than 20 keV); in this case the power law, as long as the optical depth is low and the electron temperature is not too high, is a good approximation of the Comptonized spectrum, whose *y*-parameter,

$$y = \frac{4kT_e}{m_e c^2}\,(\tau + \tau^2), \tag{3}$$

is related to the photon index of the power law by the following relation:

$$\alpha = -\frac{1}{2} + \sqrt{\frac{9}{4} + \frac{\pi^2}{3y}}\,. \tag{4}$$

In the case of Sco X-1 spectra on the HB/NB, we derived photon indexes in the 1.8–2.2 range that imply a *y* Compton parameter in the 0.6–1.1 range; a $\tau = 1$ thick plasma would then require a $\sim$50 keV thermal plasma, while a $\tau = 2$, on the contrary, would require a $\sim$15 keV electron temperature. We did not find any evidence of high-energy cutoff, obtaining only lower limits in the 50–100 keV energy range, and this constraints the optical depth to be less than 1, while the electron temperature would be greater than 50 keV. The formation of hot zones, or blobs, of very hot plasma, possibly powered by episodes of magnetic reconnection

above the disk, constitutes a plausible scenario (Haardt et al. 1994); this model has been also proposed in the case of the hard/low states of BH candidates (Malzac et al. 2004), which share with the bright *Z* source systems, from a spectral point of view, similar values of the hard photon indexes and the low accretion state, while they naturally differ from the strong boundary layer emission present in the NS sources and absent in the BH case.

A thermal origin, on the other hand, for the topFB hard tails seems to be excluded, as it would require unrealistic large values of the electron temperature.

Our analysis has shown that this scenario is statistically equivalent to a hybrid Comptonization model, in which the nonthermal fraction of the power injected in the electron heating counts up to half of the total injected power. The nonthermal fraction is significantly higher with respect to the value found by Farinelli et al. (2005) in the case of GX 17+2. The nonthermal fraction for the topFB spectra must be distinguished from the nonthermal spectra of the BH sources, as in the case of Sco X-1, the hard luminosity is a small fraction of the soft luminosity that dominates the 10–30 keV energy spectrum. Most of the soft photons do not Compton interact with the electron cloud, because of the low optical depth values.

Another possible physical mechanism to explain the hard X-ray variability is the bulk motion Comptonization (e.g., Psaltis 2001), present in systems with a high-velocity radial accretion flows. This radiation mechanism, used to explain the hard power-law component in BH systems spectra in their soft/high states, is, however, not able to account for the absence of any cutoff up to energies of 0.5 MeV and for the hard photon indexes observed ($\Gamma \leq 2.0$; Niedźwiecki & Zdziarski 2006). In the case of bright NS systems, the high radiation pressure of the inner boundary layer constitutes a strong barrier for any incoming convergent bulk motion flow. On the other hand, because jets have been observed in the radio from Sco X-1, bulk motion Comptonization inside the jet can be an important production mechanism of hard X-ray radiation also. Theoretical spectra and energetic contribution according to the relevant physical parameters involved in the case of a strict coupling with inflow (i.e., accretion to the compact object through the formation of an accretion disk) and outflow (i.e., jets) are a promising way to cover in a self-consistent way all the phases of accretion. Details about the geometry of the scattering media, amount of reflection on the cold disk, and dependence from the accretion state of the source are yet to be fully explored. Moreover, in this case synchrotron emission of soft photons by a beamed population of relativistic electrons becomes a competitive source of photons with respect to the thermal soft photon emission of the boundary layer and accretion disk. An attempt to explicitly compute a jet spectrum, from radio to hard X-rays, has been recently proposed by Markoff et al. (2005), where the jet base subsumes the role of the static Comptonizing corona; spectral fits in the case of BH systems (namely Cyg X-1 and GX 339-4) in hard states are consistent with this scenario, but BH soft states and NS systems spectra need yet to be tested in order to understand the limits of validity of the jet model.

Questions to be further addressed in future observations are: the exact shape and contribution of the soft component below the 3 keV range, the investigation with good spectral resolution in the 6–10 keV range of the reflection features, and the extension up to 0.5 MeV of the spectral coverage in order to constrain the physical parameters characterizing the nonthermal electron distribution of the Comptonizing plasma. The latter point is well within the capabilities of the recently launched *Suzaku* satellite, so that future observations in this direction can be a stringent test to our conclusions.

This work was partially supported by the Ministero dell' Università e Ricerca (MiUR). This research has made use of data obtained from the High Energy Astrophysics Science Archive Research Center (HEASARC), provided by NASA's Goddard Space Flight Center.

REFERENCES

Agrawal, P. C., Biswas, S., Gokhale, G. S., Iyengar, V. S., Kunte, P. K., Manchanda, R. K., & Sreekantan, B. V. 1971, Ap&SS, 10, 500
Asai, K., Dotani, T., Mitsuda, K., Nagase, F., Kamado, Y., Kuulkers, E., & Breedon, L. M. 1994, PASJ, 46, 479
Barnard, R., Church, M. J., & Bałucińska-Church, M. 2003, A&A, 405, 237
Bradshaw, C. F., Fomalont, E. B., & Geldzahler, B. J. 1999, ApJ, 512, L121
Bradshaw, C. F., Geldzahler, B. J., & Fomalont, E. B. 2003, ApJ, 592, 486
Brandt, W. M., & Matt, G. 1994, MNRAS, 268, 1051
Casella, P., Belloni, T., & Stella, L. 2006, A&A, 446, 579
Christian, D. J., & Swank, J. H. 1997, ApJS, 109, 177
Church, M. J., & Balucińska-Church, M. 2001, A&A, 369, 915
Coppi, P. S. 1999, in ASP Conf. Ser. 161, High Energy Processes in Accreting Black Holes, ed. J. Poutanen & R. Svensson (San Francisco: ASP), 375
———. 2000, BAAS, 32, 1217
Costantini, E., Freyberg, M. J., & Predehl, P. 2005, A&A, 444, 187
D'Amico, F., Heindl, W. A., Rothschild, R. E., & Gruber, D. E. 2001, ApJ, 547, L147
Di Salvo, T., Robba, N. R., Iaria, R., Stella, L., Burderi, L., & Israel, G. L. 2001, ApJ, 554, 49
Di Salvo, T., et al. 2000, ApJ, 544, L119
———. 2006, ApJ, 649, L91
Done, C., Życki, P. T., & Smith, D. A. 2002, MNRAS, 331, 453
Farinelli, R., Frontera, F., Zdziarski, A. A., Stella, L., Zhang, S. N., van der Klis, M., Masetti, N., & Amati, L. 2005, A&A, 434, 25
Fender, R. P. 2002, in Relativistic Flows in Astrophysics, ed. A. W. Guthmann et al. (Berlin: Springer), 101
Fender, R. P., & Hendry, M. A. 2000, MNRAS, 317, 1
Fiocchi, M., Bazzano, A., Ubertini, P., & Jean, P. 2006, ApJ, 651, 416
Fomalont, E. B., Geldzahler, B. J., & Bradshaw, C. F. 2001, ApJ, 558, 283
Giacconi, R., Gursky, H., Paolini, F. R., & Rossi, R. 1962, Phys. Rev. Lett., 9, 439
Gierliński, M., & Done, C. 2002, MNRAS, 331, L47
Gierliński, M., Zdziarski, A. A., Poutanen, J., Coppi, P. S., Ebisawa, K., & Johnson, W. N. 1999, MNRAS, 309, 496
Haardt, F., Maraschi, L., & Ghisellini, G. 1994, ApJ, 432, L95
Hasinger, G., & van der Klis, M. 1989, A&A, 225, 79
Inogamov, N. A., & Sunyaev, R. A. 1999, Astron. Lett., 25, 269
Jahoda, K., et al. 1996, BAAS, 28, 1285
Kato, Y., Hayashi, M. R., & Matsumoto, R. 2004, ApJ, 600, 338
Malzac, J., Merloni, A., & Fabian, A. C. 2004, MNRAS, 351, 253
Manchanda, R. K. 2006, Adv. Space Res., 37, 2139
Markoff, S., Nowak, M. A., & Wilms, J. 2005, ApJ, 635, 1203
Merloni, A., Fabian, A. C., & Ross, R. R. 2000, MNRAS, 313, 193
Migliari, S., Fender, R. P., Rupen, M., Jonker, P. G., Klein-Wolt, M., Hjellming, R. M., & van der Klis, M. 2003, MNRAS, 342, L67
Mitsuda, K., et al. 1984, PASJ, 36, 741
Muno, M. P., Remillard, R. A., & Chakrabarty, D. 2002, ApJ, 568, L35
Niedźwiecki, A., & Zdziarski, A. A. 2006, MNRAS, 365, 606
Poutanen, J., Nagendra, K. N., & Svensson, R. 1996, MNRAS, 283, 892
Psaltis, D. 2001, ApJ, 555, 786
Revnivtsev, M., & Gilfanov, M. 2006, A&A, 453, 253
Rothschild, R. E., et al. 1998, ApJ, 496, 538
Shimura, T., & Takahara, F. 1995, ApJ, 445, 780
Smale, A. P., et al. 1993, ApJ, 410, 796
Steeghs, D., & Casares, J. 2002, ApJ, 568, 273
Stella, L., & Vietri, M. 1999, Phys. Rev. Lett., 82, 17
Tarana, A., Bazzano, A., Ubertini, P., & Zdziarski, A. A. 2007, ApJ, 654, 494
Titarchuk, L. 1994, ApJ, 434, 570
van der Klis, M. 2006, in Compact Stellar X-Ray Sources, ed. W. Lewin & M. van der Klis (Cambridge: Cambridge Univ. Press), 39
van der Klis, M., Swank, J. H., Zhang, W., Jahoda, K., Morgan, E. H., Lewin, W. H. G., Vaughan, B., & van Paradijs, J. 1996, ApJ, 469, L1
Vierdayanti, K., Mineshige, S., Ebisawa, K., & Kawaguchi, T. 2006, PASJ, 58, 915

Vrtilek, S. D., Penninx, W., Raymond, J. C., Verbunt, F., Hertz, P., Wood, K., Lewin, W. H. G., & Mitsuda, K. 1991, ApJ, 376, 278
Wardziński, G., Zdziarski, A. A., Gierliński, M., Eric Grove, J., Jahoda, K., & Neil Johnson, W. 2002, MNRAS, 337, 829
White, N. E., Peacock, A., Hasinger, G., Mason, K. O., Manzo, G., Taylor, B. G., & Branduardi-Raymont, G. 1986, MNRAS, 218, 129
Zdziarski, A. A., Grove, J. E., Poutanen, J., Rao, A. R., & Vadawale, S. V. 2001, ApJ, 554, L45
Zdziarski, A. A., Johnson, W. N., & Magdziarz, P. 1996, MNRAS, 283, 193
Zhang, C. M., Yin, H. X., Zhao, Y. H., Zhang, F., & Song, L. M. 2006, MNRAS, 366, 1373